

1 **Integrated studies of a regional ozone pollution synthetically**  
2 **affected by subtropical high and typhoon system in the**  
3 **Yangtze River Delta region, China**

4 **Lei Shu, Min Xie<sup>\*</sup>, Tijian Wang<sup>\*</sup>, Da Gao, Pulong Chen, Yong Han, Shu Li, Bingliang**  
5 **Zhuang, Mengmeng Li**

6 School of Atmospheric Sciences, CMA-NJU Joint Laboratory for Climate Prediction Studies,  
7 Jiangsu Collaborative Innovation Center for Climate Change, Nanjing University, Nanjing 210023,  
8 China

9 -----

10 \*Correspondence to: Min Xie (minxie@nju.edu.cn) and Tijian Wang (tjwang@nju.edu.cn)

11

12 **Abstract:** Severe high ozone (O<sub>3</sub>) episodes usually have close relations to synoptic systems. A  
13 regional continuous O<sub>3</sub> pollution episode was detected over the Yangtze River Delta (YRD) region  
14 in China during August 7-12 2013, in which the O<sub>3</sub> concentrations in more than half of the cities  
15 exceeded the national air quality standard. The maximum hourly concentration of O<sub>3</sub> reached  
16 167.1 ppb. By means of the observational analysis and the numerical simulation, the  
17 characteristics and the essential impact factors of the typical regional O<sub>3</sub> pollution are integratedly  
18 investigated. The observational analysis shows that the atmospheric subsidence dominated by  
19 Western Pacific subtropical high plays a crucial role in the formation of high-level O<sub>3</sub>. The  
20 favorable weather conditions, such as extremely high temperature, low relative humidity and weak  
21 wind speed, caused by the abnormally strong subtropical high are responsible for the trapping and  
22 the chemical production of O<sub>3</sub> in the boundary layer. In addition, when the YRD cities are at the  
23 front of Typhoon Utor, the periphery circulation of typhoon system can enhance the downward  
24 airflows and cause worse air quality. But when the typhoon system weakens the subtropical high,  
25 the prevailing southeasterly surface wind leads to the mitigation of the O<sub>3</sub> pollution. The  
26 Integrated Process Rate (IPR) analysis incorporated in the Community Multi-scale Air Quality  
27 (CMAQ) Model is applied to further illustrate the combined influence of subtropical high and  
28 typhoon system in this O<sub>3</sub> episode. The results show that the vertical diffusion (VDIF) and the  
29 gas-phase chemistry (CHEM) are two major contributors to O<sub>3</sub> formation. During the episode, the

30 contributions of VDIF and CHEM to O<sub>3</sub> maintain the high values over the YRD region. On August  
31 10-12, the cities close to the sea are apparently affected by the typhoon system, with the  
32 contribution of VDIF increasing to 28.45 ppb/h in Shanghai and 19.76 ppb/h in Hangzhou. In  
33 contrast, the cities far away from the sea can hardly be affected by the periphery circulation of  
34 typhoon system. When the typhoon system significantly weakens the subtropical high, the  
35 contribution values of all individual processes decrease to a low level in all YRD cities. These  
36 results provide an insight for the O<sub>3</sub> pollution synthetically impacted by the Western Pacific  
37 subtropical high and the tropical cyclone system.

38 **Keyword:** Ozone; subtropical high; typhoon; the Yangtze River Delta region; heat wave

39

## 40 **1. Introduction**

41 Ground-level ozone (O<sub>3</sub>) is a secondary air pollutant generated by a series of complicated  
42 photochemical reactions involving nitrogen oxides (NO<sub>x</sub>) and hydrocarbons (HC) (Crutzen, 1973;  
43 Sillman, 1999; Jenkin et al., 2000; Wang et al., 2006b; Xie et al., 2014; 2016b). Severe O<sub>3</sub>  
44 pollution events usually occur in the presence of sunlight and under favorable meteorological  
45 conditions, with the abundance of O<sub>3</sub> precursors (NO<sub>x</sub> and HC) (Wang et al., 2006b). These O<sub>3</sub>  
46 pollutions in troposphere can deteriorate the air quality, and thereby cause adverse effects on  
47 human health and vegetation (Feng et al., 2003; Fann and Risley, 2013; Landry et al., 2013).  
48 Consequently, the formation mechanism and the integrated prevention of O<sub>3</sub> pollution are of great  
49 concern in many megacities all over the world (Xie et al., 2016b).

50 Over the past decades, along with the rapid industrial and economic development, many areas  
51 in China have been suffering from high levels of O<sub>3</sub> pollution. Especially in the most economically  
52 vibrant and densely populated areas, such as the Yangtze River Delta (YRD) region, the Pearl  
53 River Delta (PRD) region, and the Beijing-Tianjin-Hebei (BTH) area, the severe O<sub>3</sub> pollution  
54 episode has frequently occurred (Lam et al., 2005; Wang et al., 2006b; An et al., 2007; Chan and  
55 Yao, 2008; Duan et al., 2008; Jiang et al., 2008; Zhang et al., 2008; Guo et al., 2009; Shao et al.,  
56 2009; Ma et al., 2012) , and the background air pollutant concentrations have steadily increased  
57 (Chan and Yao, 2008; Zhang et al., 2008; Tang et al., 2009; Wang et al., 2009a; Ma et al., 2012;  
58 Liu et al., 2013). Many studies on the O<sub>3</sub> pollution, including satellite data analyses, field  
59 experiments, and model simulations, have been carried out over China in order to investigate the

60 temporal and spatial characteristics of surface photochemical pollutions (Lu and Wang, 2006;  
61 Wang et al., 2006a; Tu et al., 2007; Zhang et al., 2007; 2008; Geng et al., 2008; Tang et al., 2008;  
62 2009; Chen et al., 2009; Han et al., 2011; Ding et al., 2013; Xie et al., 2016b), nonlinear  
63 photochemistry of O<sub>3</sub> and its precursors (Lam et al., 2005; Ran et al., 2009; Liu et al., 2010; Li et  
64 al., 2011; Xie et al., 2014), interactions between O<sub>3</sub> and aerosols (Lou et al., 2014; Shi et al., 2015),  
65 the effects of urbanization on O<sub>3</sub> formation (Wang et al., 2007; 2009b; Liao et al., 2015; Li et al.,  
66 2016; Xie et al., 2016a; Zhu et al., 2016), and other essential impact factors (Jiang et al., 2012; Li  
67 et al., 2012; Wei et al., 2012; Liu et al., 2013; Gao et al., 2016).

68 The Yangtze River Delta (YRD) region is a highly developed area of urbanization and  
69 industrialization. With the accelerated economic development and remarkable increase in energy  
70 consumption, the photochemical smog with high level of O<sub>3</sub> concentration is becoming more and  
71 more prominent and frequent, tending to present the characteristics of regional pollution (Chan  
72 and Yao, 2008; Ma et al., 2012; Li et al., 2012). Being located on the southeastern coast of China,  
73 YRD features a typical subtropical monsoon climate and is strongly affected by the Western  
74 Pacific subtropical high in summer. So, high O<sub>3</sub> concentrations are usually observed in late spring  
75 and summer by in-situ monitoring (Ding et al., 2013; Xie et al., 2016b). Severe high O<sub>3</sub> episodes  
76 usually have close relations to synoptic systems (Huang et al., 2005; 2006; Wang et al., 2006b;  
77 Jiang et al., 2008; Cheng et al., 2014; Hung and Lo, 2015). Horizontal and vertical transport  
78 processes from upwind O<sub>3</sub>-rich air masses as well as poor atmospheric diffusion conditions can  
79 lead to the accumulation of surface O<sub>3</sub> concentrations and aggravating the photochemical pollution  
80 (Wang et al., 2006b). In previous studies on high O<sub>3</sub> pollution in the YRD region, some  
81 researchers have discussed this issue. For example, Jiang et al. (2012) investigated the spring O<sub>3</sub>  
82 formation over East China, and suggested that O<sub>3</sub> concentrations over the YRD region were  
83 transported and diffused from surrounding areas. Li et al. (2012) presented quantitative analysis on  
84 atmospheric processes affecting O<sub>3</sub> concentrations in the typical YRD cities during a summertime  
85 regional high O<sub>3</sub> episode, and found that the maximum concentration of photochemical pollutants  
86 was usually related with the process of transportation. Gao et al. (2016) evaluated the O<sub>3</sub>  
87 concentration during a frequent shifting wind period, and revealed that vertical mixing played an  
88 important positive role in the formation of surface O<sub>3</sub>. However, these investigations only focused  
89 on the O<sub>3</sub> formation mechanism for one megacity (such as Shanghai, Nanjing and Hangzhou, etc.)

90 or just a single station. Up to now, studies on the process analysis of high ozone episodes over the  
91 YRD are quite limited (Li et al., 2012). So, more studies should pay attention to the typical  
92 weather systems and the exact formation mechanism of the regional O<sub>3</sub> pollution in this region.

93 During August 7-12 2013, there was a typical regional O<sub>3</sub> pollution episode in the YRD  
94 region, which might be synthetically influenced by the Western Pacific subtropical high and  
95 Typhoon Utor. To better understand the important factors impacting O<sub>3</sub> formation from the  
96 regional scale, we investigated the exact roles of these two typical weather systems in this  
97 pollution episode by using observational analysis and numerical simulations. The observational  
98 analysis was performed to identify the temporal and spatial characteristics of the episode. The  
99 WRF/CMAQ modeling system, which consists of the Weather Research and Forecasting model  
100 (WRF) and the Community Multi-scale Air Quality Model (CMAQ), was used to reveal the exact  
101 formation mechanism. With the aid of the Integrated Process Rate (IPR) analysis coupled in  
102 CMAQ, the qualitative and the quantitative analysis on the contributions of individual atmospheric  
103 processes were conducted as well. In this paper, the brief description of observational data and  
104 model configurations are shown in Section 2. The detailed observational analysis of air quality and  
105 meteorological conditions are given in Section 3. The evaluation of model performance and the  
106 formation mechanism of O<sub>3</sub> explored by IPR technique are presented in Section 4. In the end, a  
107 summary of main findings is given in Section 5.

108

## 109 **2. Methodology**

### 110 **2.1 Observed meteorological and chemical data**

111 The air quality observational data are used to identify the regional characteristics of the O<sub>3</sub>  
112 episode in August 2013. Fifteen cities are selected as the representative research objects to better  
113 reflect the status of O<sub>3</sub> pollution over the YRD region. The locations of these cities are shown in  
114 Fig. 1b, which contains Shanghai, 8 cities in Jiangsu province (Changzhou, Nanjing, Nantong,  
115 Suzhou, Taizhou, Wuxi, Yangzhou, and Zhenjiang), and 6 cities in Zhejiang province (Hangzhou,  
116 Huzhou, Jiaxing, Ningbo, Shaoxing, and Zhoushan). The in-situ monitoring data for the hourly  
117 concentrations of O<sub>3</sub>, CO, NO<sub>2</sub>, SO<sub>2</sub>, PM<sub>2.5</sub> and PM<sub>10</sub> can be acquired from National  
118 Environmental Monitoring Center (NEMC) (<http://106.37.208.233:20035>). The assurance/quality  
119 control (QA/QC) procedures for monitoring strictly follow the national standards (State

120 Environmental Protection Administration of China, 2006). The hourly pollutant concentration for  
121 a city is calculated as the average of the pollutant concentrations from several national monitoring  
122 sites in that city, which can better characterize the pollution level of the city. In order to identify  
123 invalid or lacking data, a checking procedure for these data is performed following the work of  
124 Chiqueto and Silva (2010). Finally, only less than 0.2% of the primary data are ignored in the  
125 calculation. Moreover, the observed data of total VOCs (TVOC) during August 4-10 at an urban  
126 site in Shanghai (SAES, 31.17°N, 121.43°E) is also used. They are provided by Shanghai  
127 Academy of Environmental Sciences. The sampling height is about 15 m, and individual VOC  
128 species are continuously measured every 30 min by two on-line high performance gas  
129 chromatograph with flame ionization detector (GC-FID) systems (Chromato-sud airmoVOC  
130 C2-C6 #5250308 and airmoVOC C6-C12 #2260308, France). The details for measurement and  
131 QA/QC can refer to Wang et al. (2013).

132 The weather charts and the observed surface meteorological records are used to analyze the  
133 synoptic systems during the episode. The weather charts for East Asia are accessible from Korea  
134 Meteorological Administration (<http://www.kma.go.kr/chn/weather/images/analysischart.jsp>). The  
135 hourly meteorological data at the observation sites of SH (31.40°N, 121.46°E) located in Shanghai,  
136 HZ (30.23°N, 120.16°E) in Hangzhou, and NJ (32.00°N, 118.80°E) in Nanjing can be obtained  
137 from the University of Wyoming (<http://weather.uwyo.edu/wyoming/>), where 2-m air temperature,  
138 2-m relative humidity, 10-m wind speed and 10-m wind direction are available.

139 Meteorological and air quality observation data are also used to validate the reliability of  
140 simulations in this study. Comparisons of the modeling results with the observation data are  
141 performed in Shanghai, Nanjing, and Hangzhou. Shanghai is the most populous city in China, and  
142 also a global financial and transportation center. Locating to the northwest of Shanghai, Nanjing is  
143 the capital of Jiangsu Province and the second largest commercial center in East China. Hangzhou  
144 is the capital of Zhejiang Province and located to the southwest of Shanghai. These cities are the  
145 provincial capitals and the typical metropolis in the YRD region. They are highly urbanized and  
146 industrialized, and all suffer from severe O<sub>3</sub> pollution.

147

## 148 **2.2 Model description and configurations**

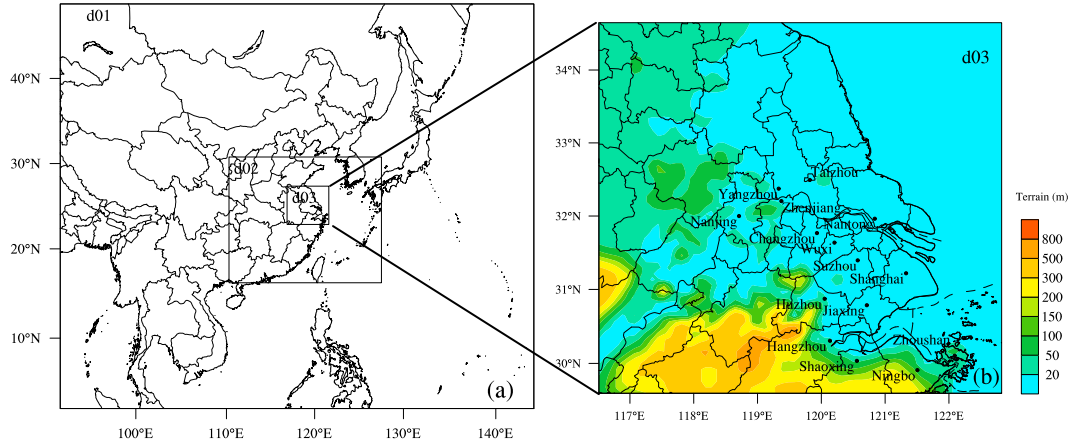
149 In this study, WRF/CMAQ, which consists of WRF model version 3.4.1 and CMAQ Model

150 version 4.7.1, is applied to simulate the high O<sub>3</sub> episode over the YRD region in August 2013.  
151 Developed at the National Center for Atmospheric Research (NCAR), WRF is a new generation of  
152 meso-scale weather forecast model and assimilation system. Numerous applications have proven  
153 that it shows a good performance in all kinds of weather forecasts and has broad application  
154 prospects in China (Jiang et al., 2008; 2012; Wang et al., 2009b; Liu et al., 2013; Xie et al., 2014;  
155 2016a; Liao et al., 2014; 2015; Li et al., 2016; Zhu et al., 2016). WRF provides off-line  
156 meteorological fields as the input for the chemical transport model CMAQ. CMAQ is a third  
157 generation of regional air quality model developed by the Environmental Protection Agency of  
158 USA (USEPA). A set of up-to-date compatible modules and control equations for the atmosphere  
159 is incorporated in the model, which can fully consider atmospheric complicated physical processes,  
160 chemical processes and the relative contribution of different species (Byun and Schere, 2006;  
161 Foley et al., 2010). CMAQ has been widely applied in China and proven to be a reliable tool in  
162 simulating air quality from city scale to meso scale (Li et al., 2012; Wei et al., 2012; Liu et al.,  
163 2013; Zhu et al., 2016).

164 The simulation run is conducted from 08:00 (local standard time, LST) on August 2 to 08:00  
165 (LST) on August 16 2013, in which the first 48 h is taken as the spin-up time. Three one-way  
166 nested domains are used in WRF with a Lambert Conformal map projection. The domain setting is  
167 shown in Fig. 1. The outermost domain (domain 1, d01) covers the most areas of East Asia and  
168 South Asia, with the horizontal grids of 88×75 and the grid spacing of 81 km. The nested domain  
169 d02 covers the southeastern part of China, with the horizontal grids of 85×70 and the grid spacing  
170 of 27 km. The finest domain (domain 3, d03) covers the core areas of the YRD region, with the  
171 grid system of 70×64 and the resolution of 9 km. For all domains, there are 23 vertical sigma  
172 layers from the surface to the top pressure of 100 hPa, with about 10 layers in the planetary  
173 boundary layer. The detailed configuration options for the dynamic parameterization in WRF are  
174 summarized in Table 1. Additionally, the SLAB scheme that does not consider urban canopy  
175 parameters is adopted to model the urban effect. In order to reflect the rapid urban expansion in  
176 the YRD region, the default United States Geological Survey (USGS) land-use archives are  
177 updated by adding the present urban land-use conditions from 500-m Moderate Resolution  
178 Imaging Spectroradiometer (MODIS) data, based on the work of Liao et al. (2014; 2015). The  
179 initial meteorological fields and boundary conditions are from 1° resolution global reanalysis data

180 provided by National Center for Environmental Prediction (NCEP). The boundary conditions are  
 181 forced every 6 h.

182



183  
 184 **Fig. 1. Domain settings, include (a) the three nested modeling domains and (b) the nested domain 3 (d03)**  
 185 **with the terrain elevations and the locations of 15 main cities in the YRD region.**

186

187 **Table 1. The grid settings and the physical options for WRF in this study.**

Items	Options
Dimensions (x, y)	(88, 75), (85, 70), (70, 64)
Grid spacing (km)	81, 27, 9
Microphysics	WRF Single-Moment 5-class scheme (Hong et al., 2004)
Longwave Radiation	RRTM scheme (Mlawer et al., 1997)
Shortwave Radiation	Goddard scheme (Kim and Wang, 2011)
Surface layer	Moni-Obukhov scheme (Monin and Obukhov, 1954)
Land-surface layer	Noah Land Surface Model (Chen and Dudhia, 2001)
Planetary Boundary layer	YSU scheme (Hong et al., 2006)
Cumulus Parameterization	Grell-Devenyi ensemble scheme (Grell and Devenyi, 2002)

188

189 With respect to the air quality model, CMAQ uses the same vertical levels and the similar  
 190 three nested domains as those adopted in the meteorological simulation, whereas the CMAQ  
 191 domains are one grid smaller than the WRF domains. The Meteorology Chemistry Interface  
 192 Processor (MCIP) is used to convert WRF outputs to the input meteorological files needed by  
 193 CMAQ. The Carbon Bond 05 chemical mechanism (CB05) (Yarwood et al., 2005) is chosen for  
 194 gas-phase chemistry, and the 4rd generation CMAQ aerosol module (Byun and Schere, 2006) is  
 195 adopted for aerosol chemistry. The initial and outmost boundary conditions are obtained from the

196 Model for Ozone and Related Chemical Tracers version 4 (MOZART-4) (Emmons et al., 2010),  
197 while those for the two nested inner domains are extracted from the immediate concentration files  
198 of their parent domains. The anthropogenic emissions are mainly from the 2012 Multi-resolution  
199 Emission Inventory for China (MEIC) with  $0.25^{\circ} \times 0.25^{\circ}$  resolution, which is re-projected for the  
200 grids of China in both domains. For the grids outside of China, the inventory developed for the  
201 Intercontinental Chemical Transport Experiment-Phase B (INTEX-B) by Zhang et al. (2009) is  
202 used. The natural  $O_3$  precursor emissions are calculated by the natural emission model developed  
203 by Xie et al. (2007; 2009; 2014), including NO from soil, VOCs from vegetations, and  $CH_4$  from  
204 rice paddies and terrestrial plants. The biomass burning emissions are acquired from the work of  
205 Xie et al. (2014; 2016a).

### 206 **2.3 Integrated Process Rate (IPR) analysis method**

207 The CMAQ modeling system contains process analysis module (PROCAN), which consists  
208 of the Integrated Process Rate (IPR) analysis and the Integrated Reaction Rate (IRR) analysis  
209 (Byun and Schere, 2006). IPR has the capability of calculating the hourly contributions of  
210 individual physical processes and the net effect of chemical reaction compared to the overall  
211 concentrations, and thereby can determine the quantitative contribution of each process in a  
212 specific grid cell. The atmospheric processes considered in IPR include the horizontal advection  
213 (HADV), the vertical advection (ZADV), the horizontal diffusion (HDIF), the vertical diffusion  
214 (VDIF), the emissions (EMIS), the dry deposition (DDEP), the cloud processes with the aqueous  
215 chemistry (CLDS), the aerosol processes (AERO) and the gas-phase chemistry (CHEM). IPR has  
216 been widely applied to investigate the regional photochemical pollutions, and proven to be an  
217 effective tool to show the relative importance of every process and provide a fundamental  
218 interpretation (Goncalves et al., 2009; Li et al., 2012; Liu et al., 2013; Zhu et al., 2016). In this  
219 paper, the period from August 4 to 15 is selected for the IPR analysis. With the aid of IPR, we  
220 assess the roles of the individual physical and chemical processes involved in  $O_3$  formation over  
221 the YRD region, and further present those in the typical cities (Shanghai, Nanjing and Hangzhou).

### 222 **2.4 Evaluation method**

223 Comparisons of the modeling results in the finest domain (d03) with the hourly observation  
224 data are performed for meteorological factors and air pollutants in Shanghai, Hangzhou, and  
225 Nanjing. The correlation coefficient (R), the normalized mean bias (NMB) and the



226 root-mean-square error (RMSE) are used to evaluate the model performance. These statistic values  
 227 are calculated as follows:

$$228 \quad R = \frac{\sum_{i=1}^N (S_i - \bar{S})(O_i - \bar{O})}{\sqrt{\sum_{i=1}^N (S_i - \bar{S})^2} \sqrt{\sum_{i=1}^N (O_i - \bar{O})^2}} \quad (1)$$

$$229 \quad NMB = \frac{\sum_{i=1}^N (S_i - O_i)}{\sum_{i=1}^N O_i} \times 100\% \quad (2)$$

$$230 \quad RMSE = \left[ \frac{1}{N} \sum_{i=1}^N (S_i - O_i)^2 \right]^{\frac{1}{2}} \quad (3)$$

231 where  $S_i$  and  $O_i$  represent the simulated and the observed value, respectively.  $N$  means the total  
 232 number of valid data. Generally, the model performance is acceptable if the values of NMB and  
 233 RMSE are close to 0 and that of R is close to 1.

234

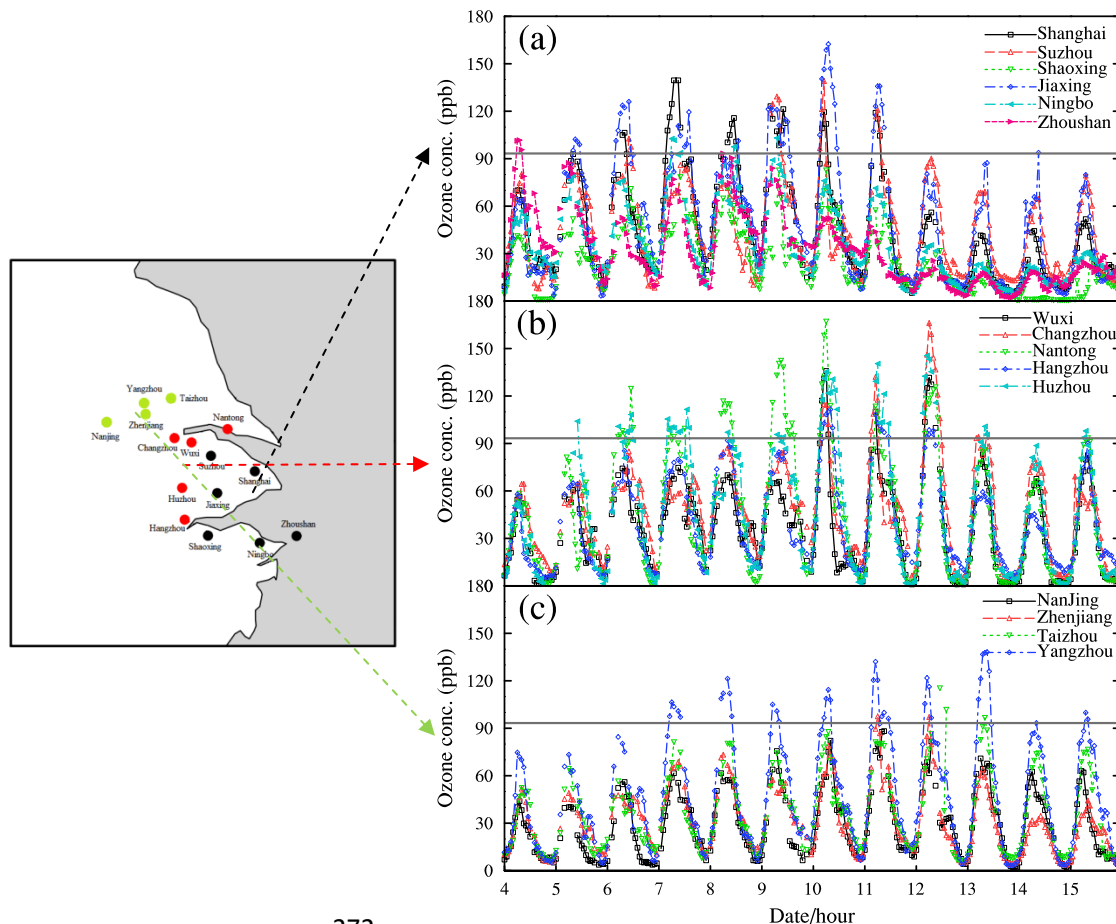
### 235 3. Characteristics of the continuous ozone episode

#### 236 3.1 Basic characteristic of the regional ozone episode in August 2013

237 Fig. 2 shows the temporal variation of the hourly  $O_3$  concentrations observed in 15 typical  
 238 cities over the YRD region from 00:00 (Universal Time Coordinated, UTC) August 4 to 23:00  
 239 (UTC) August 15 in 2013. Obviously, from August 7 to 12, high  $O_3$  concentrations over 93.5 ppb  
 240 (approximately equal to the hourly national air quality standard of  $200 \mu\text{g}/\text{m}^3$ ) have been  
 241 frequently recorded in 13 cities, which means  $O_3$  concentrations in most cities over the YRD  
 242 region exceed the national air quality standard. So, this high  $O_3$  pollution episode is a typical  
 243 regional  $O_3$  pollution episode that can affect the people and the ecosystem in a large area. In  
 244 general, for each city, there is a remarkable continuous growth in  $O_3$  concentrations before the  $O_3$   
 245 episode, followed by the lasting heavy  $O_3$  pollution period. Though the  $O_3$  concentrations in  
 246 Shaoxing and Nanjing meet the national  $O_3$  standard, their time series still show the similar  
 247 tendency to those of the other cities in the same region. The excessive level of  $O_3$  occurring in  
 248 Huzhou, Jiaxing, Nantong, Yangzhou and Shanghai lasts for more than six consecutive days,  
 249 reflecting the regional continuous characteristics of this  $O_3$  pollution episode.

250 According to the temporal variation characteristics of  $O_3$  illustrated in Fig. 2, the  
 251 abovementioned 15 typical YRD cities can be classified into three categories: (1) the cities in the

252 Southeast Coastal Region (SCR), including Shanghai, Suzhou, Jiaxing, Ningbo, Shaoxing, and  
253 Zhoushan; (2) the cities in the Central Inland Region (CIR), including Hangzhou, Huzhou, Wuxi,  
254 Changzhou, and Nantong; and (3) the cities in the Northwestern Inland Region (NIR), including  
255 Nanjing, Yangzhou, Zhenjiang, and Taizhou. The classification is primarily on basis of the  
256 observational facts that the maximum O<sub>3</sub> concentrations occur on August 10-11, 12, and 13, and  
257 begin to synchronously decrease on August 12, 13 and 14 in SCR, CIR and NIR, respectively. As  
258 shown in Fig. 2, in the Southeast Coastal Region (SCR), Zhoushan firstly exceeds the national O<sub>3</sub>  
259 standard on August 4, followed by Jiaxing, Shanghai, Suzhou and Ningbo. The peak hourly O<sub>3</sub>  
260 concentration of SCR occurs in Jiaxing on August 10, with the value up to 162.4 ppb. In the  
261 Central Inland Region (CIR), Huzhou is the first city exceeding the national O<sub>3</sub> standard, followed  
262 by the order of Nantong, Changzhou, Wuxi, and Hangzhou. The high-level O<sub>3</sub> pollution in  
263 Huzhou lasts during August 5-13. In Nantong and Changzhou, the maximum hourly O<sub>3</sub>  
264 concentration reaches 167.1 ppb on August 10 and 166.1 ppb on August 12, respectively. As for  
265 the Northwest Inland Region (NIR), Yangzhou, Zhenjiang, and Taizhou successively exceed the  
266 national O<sub>3</sub> standard. It is also noteworthy that the date when O<sub>3</sub> concentration exceeds the  
267 national air quality standard in coastal region is ahead of that in inland regions, so is the date of O<sub>3</sub>  
268 decrease. The different start time of O<sub>3</sub> decreasing in different regions might be related to the  
269 strong southeast wind in accordance with the movement of Typhoon Utor, which is discussed in  
270 Sect. 3.2 in detail.  
271



272

273 **Fig. 2. The time series of the observed  $O_3$  concentrations in 15 typical cities from August 4 to 15 2013 over**  
 274 **the YRD region, which can be divided into three areas: (a) the Southeast Coast Region (SCR), including**  
 275 **Shanghai, Suzhou, Shaoxing, Jiaxing, Ningbo, and Zhoushan; (b) the Central Inland Region (CIR),**  
 276 **including Wuxi, Changzhou, Nantong, Hangzhou, and Huzhou; (c) the Northwest Inland Region (NIR),**  
 277 **including Nanjing, Zhenjiang, Taizhou and Yangzhou. The gray solid lines in (a), (b), and (c) represent the**  
 278 **national standard for the hourly  $O_3$  concentration, which is  $200 \mu\text{g}/\text{m}^3$ .**  
 279

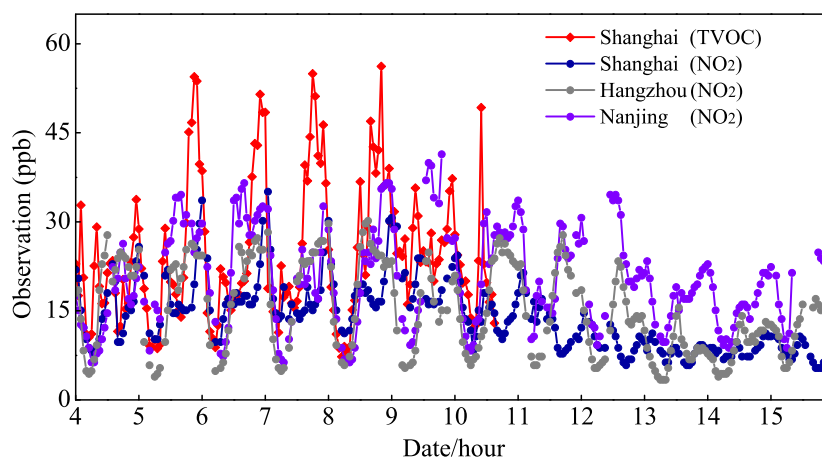
280 Table 2 presents the maximum and the average concentrations of  $O_3$  and  $\text{NO}_2$  in 15 YRD  
 281 cities during August 7-12 2013. It illustrates that the mean concentrations of  $\text{NO}_2$  in different YRD  
 282 cities range from 7.7 to 24.5 ppb during the  $O_3$  episode, indicating the heterogeneity of the spatial  
 283 distribution of  $O_3$  precursor emissions. For  $O_3$ , the highest hourly concentration (167.1 ppb)  
 284 occurs in Nantong, followed by 166.1 ppb in Changzhou and 162.4 ppb in Jiaxing. These values  
 285 are all nearly 2 times of the national air quality standard. It seems that  $O_3$  concentrations are  
 286 higher in the cities around Shanghai, where the concentrations of  $O_3$  precursors are more adequate  
 287 as well. High concentrations of  $O_3$  and its precursors imply that there may be stronger  
 288 photochemical reactions.  
 289

290 **Table 2. The maximum and average concentrations of O<sub>3</sub> and NO<sub>2</sub> observed in 15 cities during August 7-12**  
 291 **2013 (ppb).**

Sites	O <sub>3</sub>		NO <sub>2</sub>	
	Max	Mean	Max	Mean
Shanghai	139.5	55.1	35.1	15.6
Southeast	139.1	50.9	50.6	19.7
Coast	162.4	61.1	52.1	17.1
Region	113.4	41.9	31.2	12.4
(CSR)	82.6	31.9	27.8	12.7
Zhoushan	93.6	35.5	27.3	7.8
Hangzhou	111.5	48.6	30.2	16.7
Central	145.6	57.2	43.8	20.8
Inland	135.8	43.2	39.9	18.8
Region	166.1	55.7	58.4	24.5
(CIR)	167.1	56.0	48.2	20.9
Nanjing	88.2	34.1	41.4	21.9
Northwest	132.1	54.1	36.0	17.1
Inland	97.5	37.7	38.5	20.1
Region	115.3	40.5	18.5	7.7
(NIR)				

292

293 Fig. 3 demonstrates the hourly variations of the observed NO<sub>2</sub> concentrations in Shanghai,  
 294 Nanjing and Hangzhou from August 4 to 15 2013, and the time series of TVOC observed at SAES  
 295 in Shanghai from August 4 to 10 2013. Obviously, there are two peaks in the diurnal cycles of  
 296 NO<sub>2</sub> and VOC at all sites, which should be related with the rush hours in cities. The photolysis of  
 297 NO<sub>2</sub> dominates O<sub>3</sub>-VOC-NO<sub>x</sub> chemistry after 8:00, and thereby makes the concentrations of  
 298 precursors (NO<sub>2</sub> and VOC) begin to decrease. Thus, the related reactions form O<sub>3</sub> and increase its  
 299 concentration until about 14:00. These diurnal variations of O<sub>3</sub> and its precursors follow the  
 300 typical patterns in the polluted areas and reflect the close relationships between O<sub>3</sub>, VOC and NO<sub>x</sub>  
 301 (Wang et al., 2013; Xie et al., 2016b). Moreover, the daily variations of NO<sub>2</sub> and VOC show good  
 302 agreement with those of O<sub>3</sub>. For VOC, the concentration in Shanghai largely increases since  
 303 August 6, which corresponds well with the over-standard O<sub>3</sub> concentrations since then (Fig. 2).  
 304 For NO<sub>2</sub>, the higher values occur from August 6 to 11 in all cities, but the concentrations start to  
 305 decrease on August 12, 13 and 14 in Shanghai, Hangzhou and Nanjing, respectively. It seems that  
 306 the changes of O<sub>3</sub> precursors (NO<sub>2</sub> and VOC) are also affected by the movement of Typhoon Utor.



308  
 309 **Fig. 3. Temporal variations of the observed NO<sub>2</sub> concentrations at Shanghai, Nanjing and Hangzhou**  
 310 **stations from August 4 to 15 2013 and the observed TVOC concentration at SAES (31.17°N, 121.43°E) in**  
 311 **Shanghai from August 4 to 10 2013.**

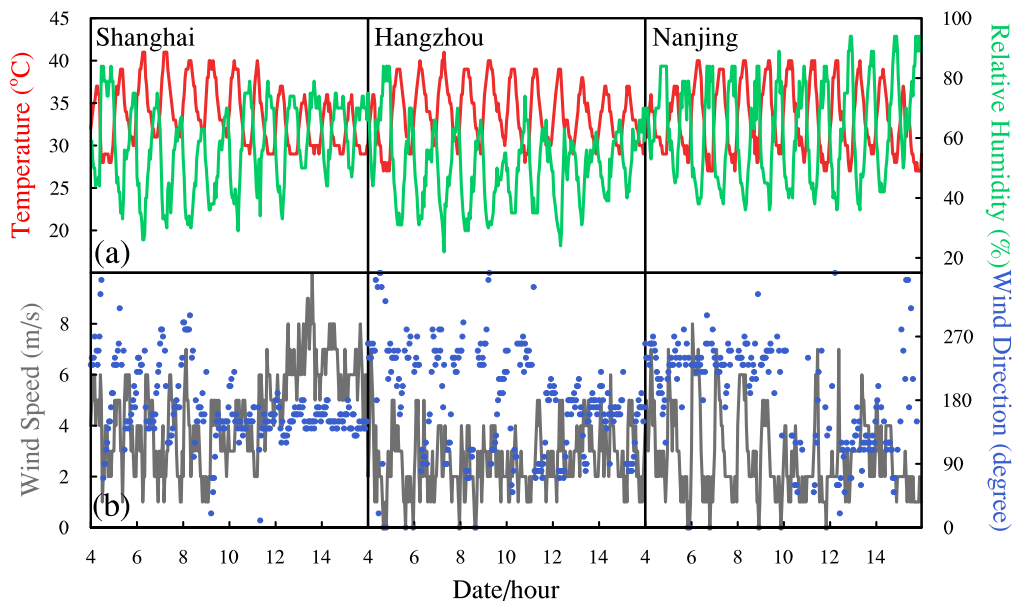
312

### 313 3.2 Meteorological condition and its effect

314 Favorable weather conditions have large impacts on the formation of severe O<sub>3</sub> pollution  
 315 (Huang et al., 2005; 2006; Wang et al, 2006b; Jiang et al., 2008; Cheng et al., 2014; Hung and Lo,  
 316 2015). High-level O<sub>3</sub> episodes often take place in hot seasons, when the meteorological conditions  
 317 with high temperature and strong solar radiation are beneficial to the photochemical reactions of  
 318 O<sub>3</sub> (Lam et al., 2005). Fig. 4 shows the variations of the surface meteorological parameters that are  
 319 related to this photochemical pollution episode during August 4-15, including 2-m air temperature,  
 320 2-m relative humidity, 10-m wind speed and 10-m wind direction at the meteorological sites in  
 321 Shanghai (SH) of SCR, Hangzhou (HZ) of CIR, and Nanjing (NJ) of NIR.

322 As shown in Fig. 4a, the hot weather at SH, HZ and NJ exists for nearly a week from August  
 323 7 to 12, with the hourly maximum temperature reaching the value over 40 °C. Meanwhile, the  
 324 variations of 2-m relative humidity show the negative correlation with those of 2-m air  
 325 temperature. The minimum 2-m relative humidity at SH and HZ occur on August 9 and August 10  
 326 respectively, with the value below 75%. These minimum values are also lower than the values  
 327 before and after the O<sub>3</sub> episode, suggesting that high-level O<sub>3</sub> episodes usually occur under the  
 328 weather conditions with high temperature and low humidity. The value of 2-m relative humidity at  
 329 NJ is relatively higher than those at SH and HZ and remains more stable. This extremely hot and

330 dry weather condition at SH, HZ, and NJ are successively relieved on August 12, 13 and 15, which  
 331 coincide well with the reduction of surface O<sub>3</sub> concentrations in Shanghai, Hangzhou, and Nanjing  
 332 (Fig. 2). With respect to the observed surface wind (Fig. 4b), the 10-m wind speed at SH and HZ is  
 333 comparatively lower during the period of the O<sub>3</sub> episode, while it is suddenly intensified after  
 334 August 12. Meanwhile, the wind direction is fluctuating from August 7 to 12, while it maintains  
 335 southeasterly wind after August 12 as well. The growth of wind speed is more distinct at SH, with  
 336 the maximum value of approximately 10 m/s. The wind speed at NJ has an obviously diurnal  
 337 variation from August 4 to 8, and the minimum value occurs on August 10.  
 338



339  
 340 **Fig. 4. Temporal variations of the main meteorological parameters at Shanghai, Hangzhou and Nanjing**  
 341 **meteorological stations during August 4-15 2013, including (a) 2-m air temperature (the red solid line) and**  
 342 **2-m relative humidity (the green solid line); (b) 10-m wind speed (the gray solid line) and 10-m wind**  
 343 **direction (the blue scatter points).**

344

345 Fig. 5 displays the weather charts for the 500 hPa layer over the East Asia at 00:00 (UTC) on  
 346 August 6, 8, 10, and 12 2013, which can illustrate the main synoptic patterns causing the O<sub>3</sub>  
 347 pollution. Obviously, during the period of the selected O<sub>3</sub> episode, the whole YRD region is under  
 348 the control of the strong Western Pacific subtropical high, which is stronger and extends much  
 349 farther west than normal. The anomaly of the subtropical high might be the direct and leading  
 350 cause of the abnormally high temperature shown in Fig. 4a (Peng et al., 2014). The intensity of the

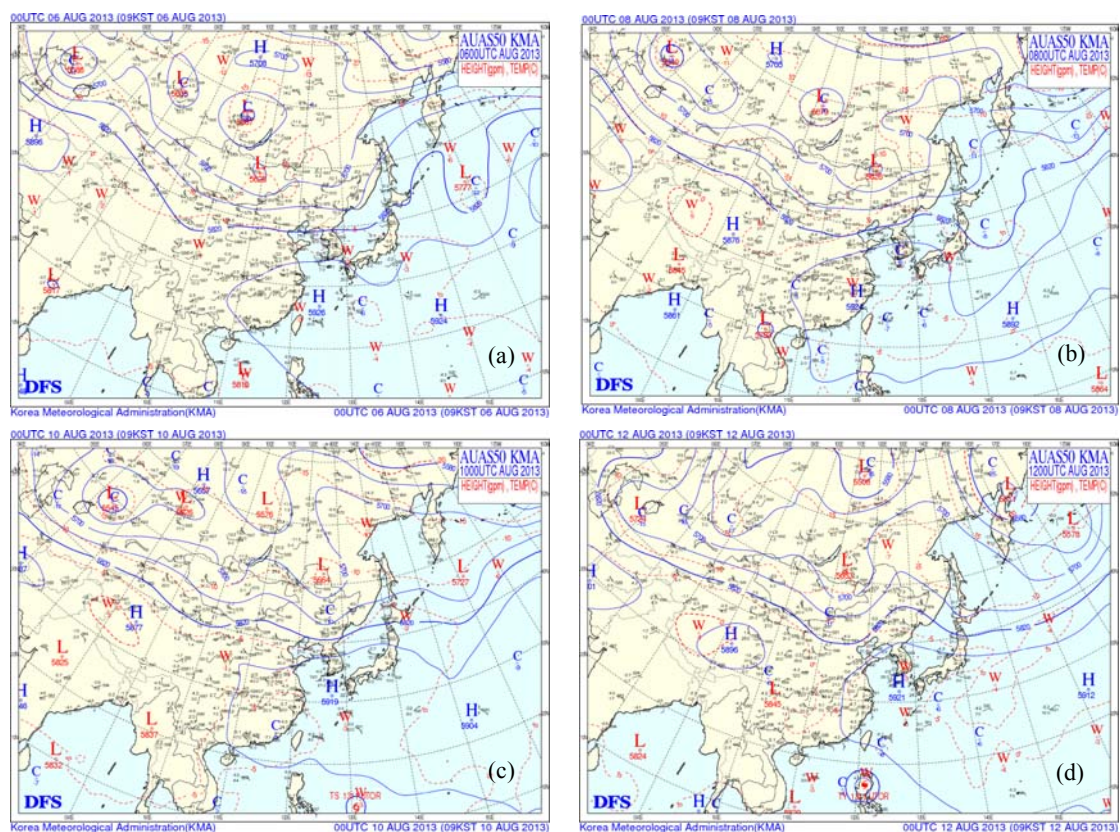
351 subtropical high is usually characterized by the area index, defined as the total number of grid  
352 points that have geopotential heights of 588 decameters or greater in the region of 110-180°E and  
353 northward of 10°N. As shown in Fig. 5, the 588-decameter area covers most of southeast China,  
354 and the high pressure center (592-decameter area) is located in the southeastern coastal areas as  
355 well as the surrounding sea areas, which means the subtropical high is very intensive. This high  
356 pressure strengthens and remains over the YRD region for several days (from August 6 to 12),  
357 implying that the air subsides to the ground. The downward air acts as a dome capping the  
358 atmosphere, and helps to trap heat as well as air pollutants at the surface. Without the lift of air,  
359 there is little convection and therefore little cumulus clouds or rains. The end result is a continual  
360 accumulating of solar radiation and heat on the ground, which may greatly enhance the  
361 photochemical reactions between the abundant build-up air pollutants.

362 The other weather system worthy of note is Typhoon Utor (shown in Fig. 5c and d). Typhoon  
363 Utor is one of the strongest typhoons in the 2013 Pacific typhoon season. It is formed early on  
364 August 8, develops into a tropical storm on August 9, undergoes an explosive  
365 intensification within a half of day, and achieves typhoon status on early August 10. After landing  
366 in Luzon of the Philippines on late August 11, it reemerges in the South China Sea on August 12.  
367 Typhoon Utor hits the land of Guangdong Province in China on August 14, and thereby is finally  
368 weakened into a tropical storm. In the end, it is ultimately dissipated on August 18. It was reported  
369 that ozone episodes during the hot season are usually associated with the passage of tropical  
370 cyclones close to the territory (Huang et al., 2005; Wang et al., 2006b; Jiang et al., 2008; Cheng et  
371 al., 2014; Hung and Lo, 2015). When a site is at the front of moving typhoon system, it can be  
372 controlled by the downward airflow induced by the typhoons' peripheral circulation. So, the  
373 typhoon system can cause the local weather around the site with high temperature, low humidity,  
374 strong solar radiation and small wind for a short time, before it is close enough to bring winds and  
375 rains. All these changes of meteorological conditions can help to form the severe continuous O<sub>3</sub>  
376 pollution (Jiang et al., 2008). In this O<sub>3</sub> episode, the YRD region may be influenced by the  
377 peripheral circulation of Typhoon Utor as well. Especially on August 10-11, the downward airflow  
378 in the troposphere is significantly strengthened (shown in Fig. 7), which may enhance the build-up  
379 of heat and air pollutants, and thereby result in worse air quality shown in Fig. 2.

380 Moreover, with the approaching of Typhoon Utor from August 12 to 14, the near-surface

381 breeze over the YRD region gradually turns to be the prevailing southeasterly or southerly wind  
 382 (Fig. 5d), with the highest wind speed up to 6-10 m/s in Shanghai (Fig. 4). The strengthened wind  
 383 can bring the clean marine air from ocean to inland, and thereby effectively mitigate the O<sub>3</sub>  
 384 pollution. Meantime, Typhoon Utor also gradually affects the position and strength of the Western  
 385 Pacific subtropical high. As the typhoon continuously approaching and finally landing on  
 386 Guangdong, the high pressure system is forced to retreat easterly and move northwards. When the  
 387 high pressure center completely moves to the oceans, the YRD region is totally under the control  
 388 of the typhoon system. In the end, the hot weather is relieved and the O<sub>3</sub> pollution is mitigated.  
 389 The coastal cities in CSR are closer to the typhoon system, so they are firstly influenced during  
 390 this period. Thus, the wind at SH in CSR firstly changes, followed by HZ in CIR and NJ in NIR.  
 391 In the same way, 2-m air temperature and O<sub>3</sub> concentrations also successively decrease from  
 392 southeast (SH in CSR) to northwest (NJ in NIR) owing to the scavenging effect.

393



394 Fig. 5. Weather charts at the 500 hPa layer over the East Asia at 00:00 (UTC) on (a) August 6, (b) August 8,  
 395 (c) August 10, and (d) August 12 2013 (from Korea Meteorological Administration).

396

397 **4 Modeling results and discussions**



#### 398 4.1 Evaluation of model performance

399 To evaluate the simulation performance, the hourly modeling results during the period of  
400 August 4-15 2013 are compared with the observation records. Table 3 presents the performance  
401 statistics, including the values of the correlation coefficient (R), the normalized mean bias (NMB),  
402 and the root-mean-square error (RMSE), which are all calculated for 2-m air temperature ( $T_2$ ),  
403 2-m relative humidity ( $RH_2$ ), 10-m wind speed ( $W_{spd10}$ ), 10-m wind direction ( $W_{dir10}$ ), surface  
404 ozone concentrations ( $O_3$ ), and surface nitrogen dioxide concentrations ( $NO_2$ ) in Shanghai (SH),  
405 Nanjing (NJ), and Hangzhou (HZ).

406 As indicated in Table 3, the simulated results of surface air temperature and relative humidity  
407 from WRF show good agreement with the observations. The highest correlation coefficient of 2-m  
408 air temperature ( $T_2$ ) is found to be 0.91 at SH, followed by 0.84 at NJ and 0.80 at HZ (statistically  
409 significant at 95% confident level). The corresponding correlation coefficients for 2-m relative  
410 humidity ( $RH_2$ ) are 0.85, 0.83 and 0.78, respectively. The values of RMSE for  $T_2$  at SH, NJ and  
411 HZ are 4.15, 2.91 and 3.09 °C, and those for  $RH_2$  are 19.3%, 9.41% and 13.96%, respectively. Our  
412 simulation underestimates  $T_2$  and overestimates  $RH_2$  to some certain extent, with the values of  
413 NMB for  $T_2$  at SH, NJ and HZ being -5.68%, -5.98% and -6.53%, and those for  $RH_2$  being  
414 12.64%, 4.52% and 16.36%. These biases might be attributed to the uncertainty caused by the  
415 SLAB scheme, which can underestimate temperature in summer (Liao et al., 2014). However,  
416 according to the relevant studies (Li et al., 2012; Liao et al., 2015; Xie et al., 2016a), this level of  
417 over- or under-estimation is still acceptable. The wind components are closely related to the  
418 transport processes. As shown in Table 3, our modeling results of wind speed and direction  
419 basically reflect the characteristics of wind fields. For 10-m wind speed ( $W_{spd10}$ ), R is 0.77 at SH,  
420 0.74 at NJ, and 0.75 at HZ, respectively. Though the values of NMB (1.53%, 5.92%, and 9.21%)  
421 and RMSE (2.18, 2.41 and 2.39) display that the simulated wind speeds are a little overestimated,  
422 the biases are still reasonable and acceptable. For 10-m wind direction ( $W_{dir10}$ ), the simulated  
423 values also fit the observation records well, with the R values of 0.63 at SH, 0.57 at NJ and 0.58 at  
424 HZ. Comparing the mean values from SIM and OBS, we can find that WRF model generally  
425 simulates the prevailing wind direction during this period. In summary, the abovementioned  
426 performance statistics numbers illustrate that the WRF simulation can reflect the major  
427 characteristics of meteorological conditions of this  $O_3$  episode, and the meteorological outputs can

428 be used in the pollutant concentration simulation.

429

430 **Table 3. Comparisons between the simulations and the observations at Shanghai, Nanjing and Hangzhou**  
 431 **stations during August 4-15 2013.**

Sites <sup>a</sup>	Vars <sup>b</sup>	Mean		R <sup>e</sup>	NMB <sup>f</sup>	RMSE <sup>g</sup>
		OBS <sup>c</sup>	SIM <sup>d</sup>			
SH	T <sub>2</sub> (°C)	33.27	31.38	0.91	-5.68%	4.15
	RH <sub>2</sub> (%)	57.91	65.23	0.85	12.64%	19.3
	Wspd <sub>10</sub> (m s <sup>-1</sup> )	4.59	4.66	0.77	1.53%	2.18
	Wdir <sub>10</sub> (°)	176.34	182.57	0.63	3.53%	41.44
	O <sub>3</sub> (ppb)	87.77	82.5	0.81	-6.00%	38.79
	NO <sub>2</sub> (ppb)	29.01	38.25	0.54	31.85%	28.95
NJ	T <sub>2</sub> (°C)	32.95	30.98	0.84	-5.98%	2.91
	RH <sub>2</sub> (%)	63.28	66.14	0.83	4.52%	9.41
	Wspd <sub>10</sub> (m s <sup>-1</sup> )	3.21	3.4	0.74	5.92%	2.41
	Wdir <sub>10</sub> (°)	197.68	194.58	0.57	-1.57%	71.19
	O <sub>3</sub> (ppb)	69.7	78.15	0.81	12.12%	36.8
	NO <sub>2</sub> (ppb)	41.44	40.09	0.61	-3.26%	22.4
HZ	T <sub>2</sub> (°C)	33.25	31.08	0.8	-6.53%	3.09
	RH <sub>2</sub> (%)	52.76	61.39	0.78	16.36%	13.96
	Wspd <sub>10</sub> (m s <sup>-1</sup> )	3.04	3.32	0.75	9.21%	2.39
	Wdir <sub>10</sub> (°)	186.45	186.2	0.58	-0.13%	69.44
	O <sub>3</sub> (ppb)	76.57	84.51	0.83	10.37%	33.95
	NO <sub>2</sub> (ppb)	31.06	27.21	0.66	-12.40%	16.86

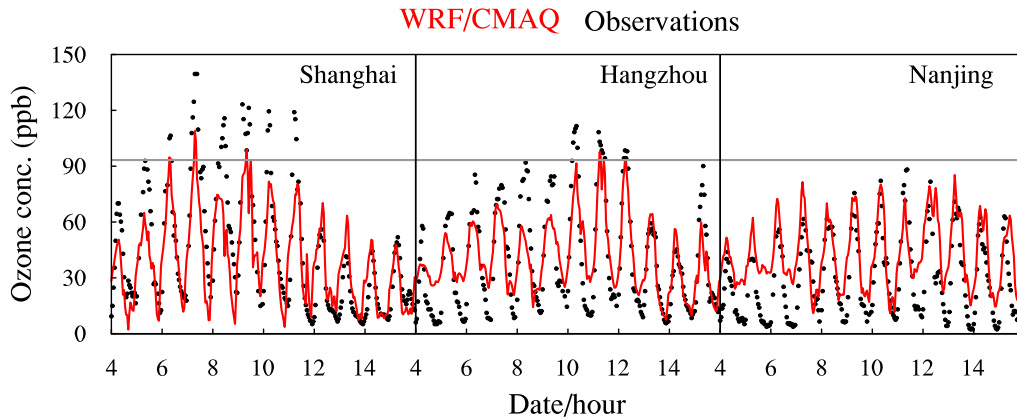
432 <sup>a</sup> Sites indicates the city where the observation sites locate, including Shanghai (SH), Nanjing (NJ), and Hangzhou  
 433 (HZ); <sup>b</sup> Vars indicates the variables under validation, including 2-m air temperature (T<sub>2</sub>), 2-m relative humidity  
 434 (RH<sub>2</sub>), 10-m wind speed (Wspd<sub>10</sub>), 10-m wind direction (Wdir<sub>10</sub>), ozone (O<sub>3</sub>), and nitrogen dioxide (NO<sub>2</sub>). The  
 435 words between the parentheses behind variables indicate the unit; <sup>c</sup> OBS indicates the observation data; <sup>d</sup> SIM  
 436 indicates the simulation results from WRF/CMAQ; <sup>e</sup> R indicates the correlation coefficients, with statistically  
 437 significant at 95% confident level; <sup>f</sup> NMB indicates the normalized mean bias; <sup>g</sup> RMSE indicates the  
 438 root-mean-square error.

439

440 Fig. 6 shows the comparisons between the modeling results from CMAQ and the observed  
 441 hourly concentrations of O<sub>3</sub> in Shanghai, Nanjing, and Hangzhou during August 4-15 2013.  
 442 Obviously, the observations and the simulated results present reasonable agreement at each site,  
 443 with the correlation coefficients of 0.81 to 0.83, NMB of -6% to 12.12%, RMSE of 33.95 to 38.79  
 444 ppb. Moreover, the simulation also reproduces the diurnal variation of O<sub>3</sub>, which shows that the  
 445 concentration reaches its maximum at around noon time and gradually decreases to its minimum

446 after midnight. With respect to the O<sub>3</sub> precursor, comparisons of NO<sub>2</sub> concentrations between  
447 simulation results and observations show that the correlation coefficient at each city is about 0.6  
448 (given in Table 3), which further prove that the process of O<sub>3</sub> formation is captured reasonable  
449 well over the YRD region and throughout the episode. However, CMAQ overestimates NO<sub>2</sub> and  
450 underestimates O<sub>3</sub> in Shanghai, while underestimates NO<sub>2</sub> and overestimates O<sub>3</sub> in Nanjing and  
451 Hangzhou. These biases of O<sub>3</sub> and NO<sub>2</sub> should mainly be attributed to the uncertainties in  
452 emissions of O<sub>3</sub> precursors (NO<sub>x</sub> and VOC<sub>s</sub>) (Li et al., 2012; Liao et al., 2015; Xie et al., 2016).  
453 Because of the VOC-sensitive O<sub>3</sub> chemistry in the daytime and NO<sub>x</sub> titration at night in the YRD  
454 region (Xie et al., 2014), higher estimation of NO<sub>x</sub> emission in Shanghai may lead to higher NO<sub>2</sub>  
455 and lower O<sub>3</sub> predictions, while lower NO<sub>x</sub> estimations in Nanjing and Hangzhou may result in  
456 lower NO<sub>2</sub> and higher O<sub>3</sub> modeling results. The undervalued NO<sub>2</sub> and overvalued O<sub>3</sub> in Nanjing  
457 and Hangzhou can also be related with the overestimations in WS<sub>10</sub> and the negative biases in T<sub>2</sub>.  
458 Moreover, the uncertainties in nonlinear chemical reactions coupled in CMAQ may also have  
459 important effects on model predictions. For example, the modeling results cannot catch the low O<sub>3</sub>  
460 values observed at night in Nanjing and Hangzhou (Fig. 6), implying there may be some  
461 imperfections in the nocturnal chemistry of CMAQ. Nevertheless, the performance of CMAQ  
462 model is comparable to the other applications (Goncalves et al., 2009; Li et al., 2012; Zhu et al.,  
463 2016). Compared to these previous related studies, the simulation in this study attains an  
464 acceptable and satisfactory result. Thus, the consistency of simulation and observation  
465 demonstrates that the modeling results are capable of capturing and reproducing the characteristics  
466 and changes of photochemical pollutants, and can be used to provide valuable insights into the  
467 governing processes of this O<sub>3</sub> episode.

468



469  
470

471 **Fig. 6. Hourly variations of the observed and the simulated O<sub>3</sub> concentrations in Shanghai, Nanjing, and**  
472 **Hangzhou during August 4 to 15 2013. The red solid lines show the modeling results, the black dot lines give**  
473 **the observations, and the solid gray lines represent the national standard for the hourly O<sub>3</sub> concentration,**  
474 **which is 200 µg/m<sup>3</sup>.**

475

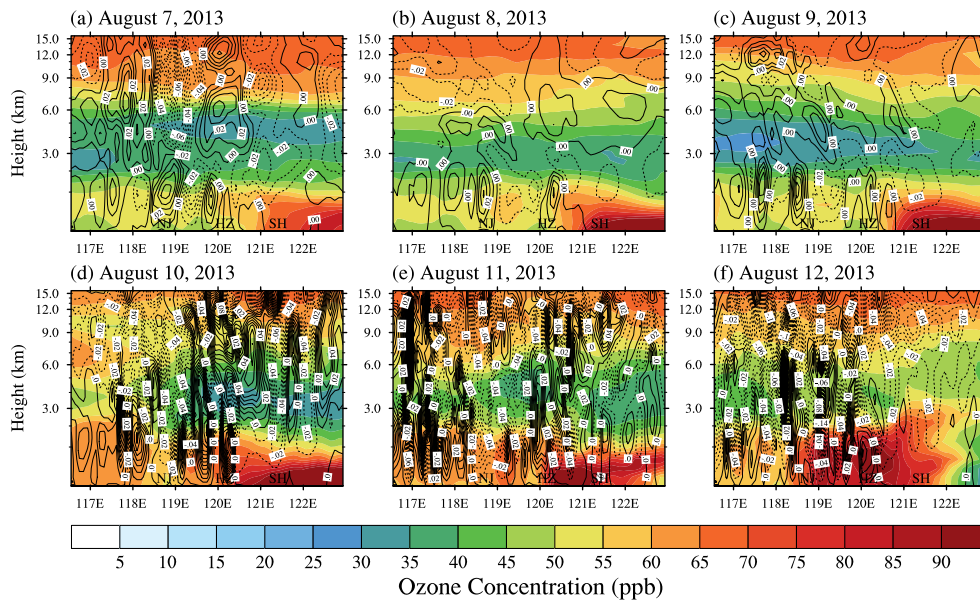
#### 476 4.2 Characteristics of the vertical airflows

477 Fig. 7 presents the daytime vertical wind velocity as well as the vertical distribution of O<sub>3</sub>  
478 concentrations from 116.5°E to 122.9°E along the latitude of 31.40°N (where Shanghai is located)  
479 during August 7-12 2013. The simulation results clearly illustrate that there are strong downward  
480 airflows over the YRD region during the period of the regional high-level O<sub>3</sub> pollution, which can  
481 be attributed to the fact that these areas are under the control of the subtropical high and the  
482 sinking airflow is predominant (as discussed in Sect. 3.2).

483 From August 7 to 9 2013, except for the mentioned regional sinking airflows, there are still  
484 some local thermal circulations continually occurring at the lower atmospheric layers (< 2 km)  
485 along the vertical cross-section of Hangzhou (HZ) - Nanjing (NJ). These circulations are related  
486 with urban heat islands. Usually high pressures are accompanied by more stagnant and fair dry  
487 weather, so the upward and the downward flows caused by urban-breeze circulations can easily  
488 appear in the urban areas. For the vertical distribution of O<sub>3</sub>, its high concentrations (> 50 ppb)  
489 generally appear from the surface to 1.5 km height above the cities. As discussed in Sect. 3.2, air  
490 pollutants tend to be trapped on the ground due to the regional sinking airflows. Moreover, the  
491 local circulations over the cities make the urban areas to be the convergence zones, and thereby  
492 more air pollutants can be accumulated in and around these cities. Under the weather conditions  
493 induced by the subtropical high, such as high air temperature, stronger solar radiation and less

494 water vapor, the chemical reactions between the build-up air pollutants can be enhanced to form  
 495 the high-level O<sub>3</sub> pollution. Additionally, Fig. 7a-c also show that there are maximum O<sub>3</sub>  
 496 concentrations (> 90 ppb) occurring near the surface in and around SH. This phenomenon should  
 497 be explained by the fact that the coastal city (SH) is firstly affected by Typhoon Utor

498 From August 10 to 12, with the approaching of Typhoon Utor, the vertical air movements  
 499 over the YRD region are not restricted at the lower atmosphere any more. As shown in Fig. 7d-f,  
 500 there are stronger downward airflows from the surface to the top of troposphere. As discussed in  
 501 Sect. 3.2, the YRD cities are at the front of the moving typhoon system, so the peripheral  
 502 circulation of Typhoon Utor may enhance the sinking of atmosphere, which can lead to higher air  
 503 temperature, lower humidity, and stronger solar radiation. Affected by the enhanced downward air  
 504 movement as well as the relevant changes of meteorological conditions, O<sub>3</sub> concentrations over  
 505 the YRD region maintain a high pollution level, with the O<sub>3</sub> concentrations over 60 ppb below the  
 506 height of 1.5 km (Fig. 7d-f). Furthermore, the high value center of O<sub>3</sub> concentrations (> 90 ppb)  
 507 moves westwards during August 10-12, implying that the peripheral circulation of Typhoon Utor  
 508 can drive the air from the coastal areas to the inland areas.  
 509



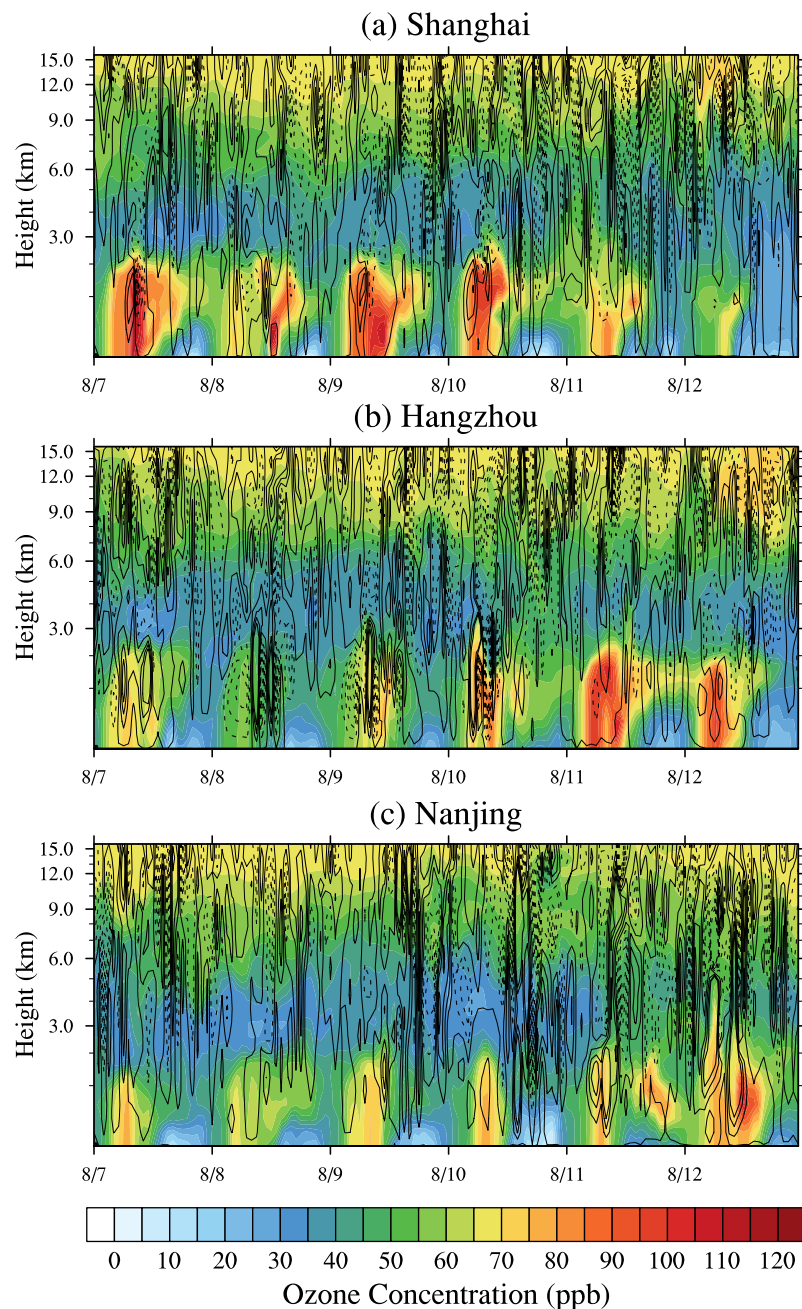
510

511 **Fig. 7. Simulated daytime vertical wind velocity and vertical distribution of O<sub>3</sub> concentrations from 116.5°E**  
 512 **to 122.9°E along the latitude of 31.40°N (where Shanghai is located) during August 7 to 12 2013. The marks**  
 513 **of SH, HZ and NJ point out the longitudes of Shanghai, Hangzhou, and Nanjing, respectively. The dotted**  
 514 **lines show the negative wind speeds and represent downward airflow, while the solid lines show the positive**  
 515 **wind speeds and zero vertical velocity. The interval is 0.01 m/s.**

516

517       The vertical changes of wind velocity and O<sub>3</sub> concentrations above Shanghai, Hangzhou and  
518 Nanjing are further illustrated in Fig. 8. Similarly, the atmospheric subsidence can also be found in  
519 the troposphere (usually occur at more than 1 km above the surface) during the period of the  
520 high-level O<sub>3</sub> pollution. With respect to Shanghai, affected by the extremely high temperature,  
521 more active photochemical reactions lead to higher O<sub>3</sub> concentrations in the whole atmospheric  
522 boundary layer. The downward airflows induced by the subtropical high trap and enhance the  
523 accumulation of surface O<sub>3</sub> as time passes. Thus, high O<sub>3</sub> concentrations are formed below 2 km  
524 above the urban areas of Shanghai, and the high concentration centers occur near the surface  
525 below 500 m. It is interesting that O<sub>3</sub> concentration on August 8 is comparatively lower, which can  
526 be seen in Fig. 2 as well. This phenomenon can be explained by the fact that the transient upward  
527 airflow occurs at above 300 m over Shanghai and inhibits the accumulation of the O<sub>3</sub> pollution at  
528 the surface (shown in Fig. 8a). Additionally, Fig. 8a also presents the possible effects of Typhoon  
529 Utor on the formation of O<sub>3</sub>. On August 10, when the typhoon system approaches to the eastern  
530 coastal areas of China, the sinking air above Shanghai is apparently strengthened, and thereby  
531 enhances the intensity of O<sub>3</sub> pollution as well as the scope of the pollution. But after August 12,  
532 when Typhoon Utor changes the wind and even impacts the subtropical high, high temperature is  
533 alleviated and the build-up O<sub>3</sub> is transported to other places. Thus, the pollution is mitigated. As to  
534 Hangzhou (Fig. 8b), from August 7 to 9, owing to weaker photochemical reactions, lower O<sub>3</sub>  
535 concentrations than that in Shanghai are found in the boundary layer. However, the O<sub>3</sub>  
536 concentration can exceed the national standard from August 10 to 12 (Fig. 2), which should be  
537 influenced by the typhoon system. The influence process is similar to the above discussion for  
538 Shanghai, that is, the upper downward airflows (over 1 km above the surface) are enhanced  
539 significantly since August 10. But for Nanjing, the O<sub>3</sub> concentration does not exceed the national  
540 O<sub>3</sub> standard during August 7-12 (Fig. 2 and 8), which should be attributed to the fact that Nanjing  
541 is far away from the coastal areas and thereby hardly affected by the downward flow in the  
542 typhoon periphery. Though the O<sub>3</sub> concentration in Nanjing increases on August 12, it should  
543 mainly be caused by the local photochemical reactions because the vertical movement below 2 km  
544 above Nanjing is dominated by upward airflows.

545



547

548 **Fig. 8. Temporal variations of the vertical wind velocity and the vertical distribution of O<sub>3</sub> concentrations**  
 549 **above (a) Shanghai, (b) Hangzhou and (c) Nanjing during August 7 to 12 2013. The dotted lines show the**  
 550 **negative wind speeds and represent the downward airflows, while the solid lines show the positive wind**  
 551 **speeds and zero vertical velocity. The interval is 0.005 m/s.**  
 552

553 It is also should be mentioned that the near-surface vertical velocities around these cities are  
 554 much lower than those at higher altitudes (Fig. 8). Especially in the planetary boundary layer (< 1  
 555 km), lots of zero-velocity lines appear near the ground. This phenomenon may be related with the  
 556 upward airflow caused by Urban Heat Islands. Thus, the maximum centers of O<sub>3</sub> occur near the  
 557 surface below 500 m, and the vertical diffusion process plays a more important role in the

558 accumulation of surface O<sub>3</sub>. The essential role of the vertical diffusion process in the O<sub>3</sub> episode is  
559 similar to that reported by Zhu et al. (2015).

560

### 561 **4.3 Process analysis for ozone formation**

#### 562 **4.3.1 Typical cities in the YRD region**

563 Fig. 9 shows the daytime mean contributions of different atmospheric processes to the  
564 formation of O<sub>3</sub> in Shanghai (SH), Nanjing (NJ), and Hangzhou (HZ) at the first modeling layer  
565 from August 4 to 15 2013. As shown in the figure, for all cities during this period, the major  
566 contributors to high O<sub>3</sub> concentrations include the vertical diffusion (VDIF), the dry deposition  
567 (DDEP), the gas-phase chemistry (CHEM), and the total advection (TADV). TADV is the sum of  
568 the horizontal advection (HADV) and the vertical advection (ZADV). In this study, HADV and  
569 ZADV are considered together as TADV because they are inevitably linked as the inseparable  
570 parts of air circulation. As discussed in Sect. 3.2, the strong sinking air causes slow wind on the  
571 ground and little clouds in the sky, so the contributions of horizontal diffusion (HDIF) and cloud  
572 processes (CLDS) are quite small during this episode.

573 In the first layer of the urban areas of Shanghai (Fig. 9a), the averaged contributions from the  
574 vertical diffusion (VDIF), the gas-phase chemistry (CHEM), the advection process (TADV), and  
575 the dry deposition (DDEP) during the daytime of August 4-15 are 9.95, 10.10, -11.74 and -7.28  
576 ppb/h, respectively. Obviously, VDIF and CHEM exhibit significant positive contributions to O<sub>3</sub>  
577 during most days, while TADV and DDEP mainly show the consumption contributions. The  
578 sinking air caused by the weather system discussed in Sect. 3.2 can trap heat and air pollutants on  
579 the ground, and make VDIF be the most import source of surface O<sub>3</sub>. Meanwhile, the hotter and  
580 dryer weather with more sunshine, above 40 °C and comparatively low relative humidity (shown  
581 in Fig. 4), which is related with the sinking air, can enhance the photochemical reactions. So,  
582 CHEM can form more O<sub>3</sub> on the ground. Compared with the time series of CHEM and DDEP in  
583 which there are no obvious fluctuations, the values of VDIF and TADV significantly change with  
584 the time, with the daytime mean contributions varying from 3.99 to 28.45 ppb/h for VDIF and  
585 from -2.56 to -28.13 ppb/h for TADV. These time variations should be related with the changes of  
586 vertical air movement. For example, the value of VDIF on August 8 is only 3.99 ppb/h, which can  
587 be attributed to the local transient upward airflow over Shanghai (shown in Fig. 8a). On August 10,



588 however, VDIF can contribute 28.45 ppb O<sub>3</sub> per hour, which may be related with the enhanced  
589 downward air movement caused by the peripheral circulation of Typhoon Utor. Moreover, during  
590 the high-level O<sub>3</sub> episode from August 7-12, the mean values for VDIF, CHEM, TADV and DDEP  
591 are 13.41, 11.21, -8.37 and -14.74 ppb/h. But after August 12, the mean contributions of VDIF,  
592 CHEM, TADV and DDEP decrease to 5.35, 9.53, -5.52 and -10.85 ppb/h. These reductions should  
593 be related with the process that the subtropical high moves eastward and northward forced by  
594 Typhoon Utor (Fig. 5d). By quantifying the relative importance of each process to O<sub>3</sub> formation,  
595 the IPR analysis provides a fundamental explanation for the synthetical influence of the high  
596 pressure and the typhoon system, which has been discussed in Sect. 3.2 and 4.1, and further  
597 illustrates the exact mechanism.

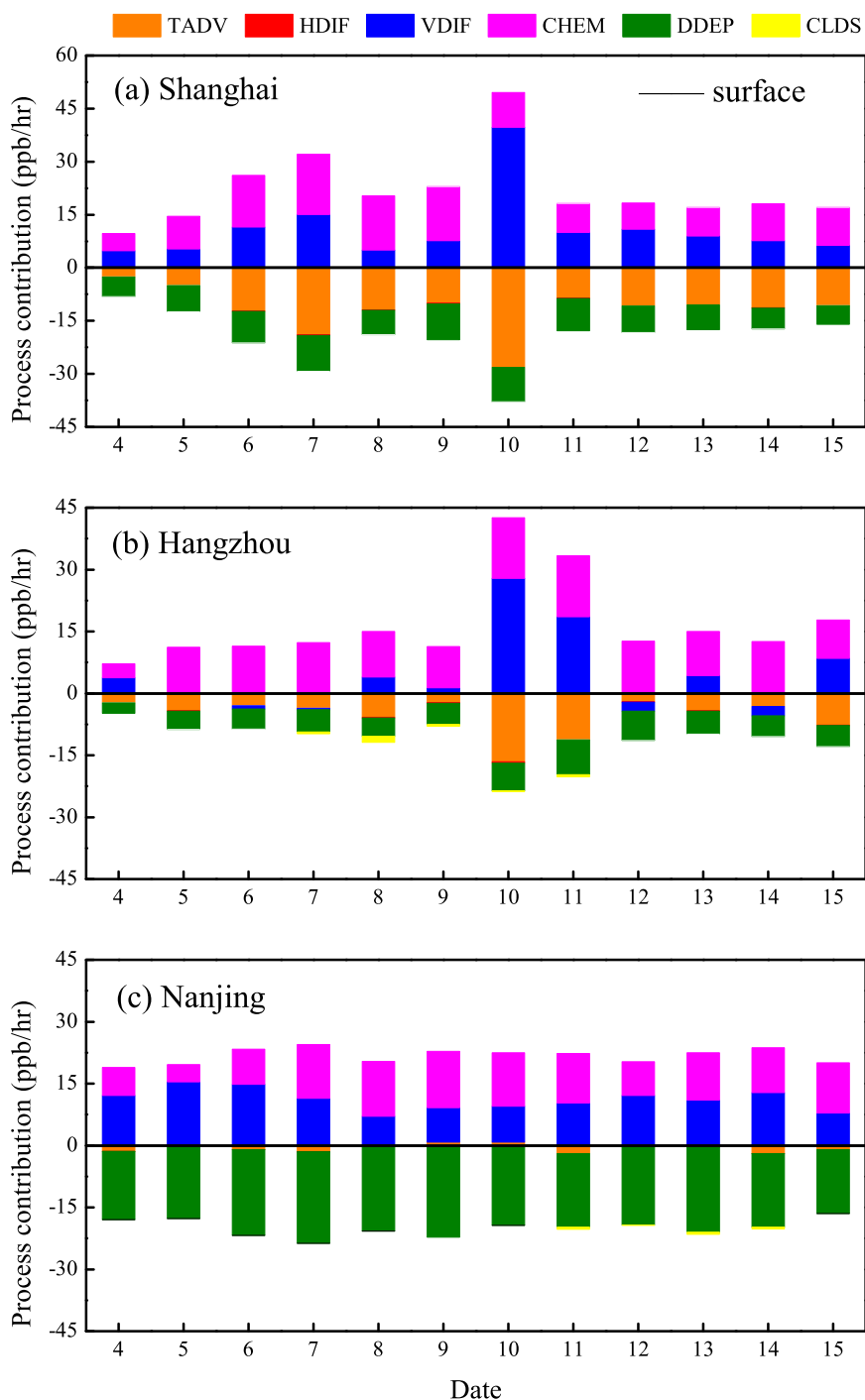
598 Fig. 9b presents the result of IPR analysis for Hangzhou. During August 4-15, VDIF and  
599 CHEM are the major source of surface O<sub>3</sub> with the average contribution of 5.36 ppb/h for VDIF  
600 and 10.97 ppb/h for CHEM, while TADV and DDEP are two important sinks for O<sub>3</sub> with the  
601 average contribution of -9.63 ppb/h for TADV and -5.14 ppb/h for DDEP. Synthetically impacted  
602 by Western Pacific subtropical high and Typhoon Utor, the mean contributions during the O<sub>3</sub>  
603 episode (from August 7 to August 12) for VDIF, CHEM, TADV and DDEP increase to 7.21, 12.61,  
604 -11.51 and -5.92 ppb/h, respectively. The highest VDIF contribution occurs on August 10-11, and  
605 the over-standard of O<sub>3</sub> concentration appears on August 10-12 as well, which may be attributed to  
606 the effect of typhoon's peripheral circulation, implying Typhoon Utor also plays an essential role  
607 in the formation of O<sub>3</sub> pollution in Hangzhou. After Typhoon Utor approaches close enough to  
608 Hangzhou, the wind direction is mainly dominated by the southeast wind (Fig. 4b), and the mean  
609 values of VDIF, CHEM, TADV and DDEP finally decrease to 4.84, 10.08, -8.92 and -4.78 ppb/h,  
610 respectively. In a word, Hangzhou is located close to Shanghai, so the temporal variations of VDIF,  
611 CHEM, TADV and DDEP in Hangzhou are similar to those in Shanghai.

612 However, the similar variation pattern of VDIF, CHEM, TADV and DDEP occurring in  
613 Shanghai and Hangzhou does not appear in Nanjing. As shown in Fig. 9c, the mean contributions  
614 of VDIF, CHEM, TADV and DDEP to surface O<sub>3</sub> in Nanjing are 11.31, 9.55 -1.34 and -17.57  
615 ppb/h during the whole period, while the values during 7-12 August are 10.32, 10.70, -0.99 and  
616 -18.42 ppb/h. There are no apparent fluctuations or sudden increases of these contributors during  
617 the period from August 4 to 15, so are the O<sub>3</sub> concentration (Fig. 2), temperature and relative

618 humidity (Fig. 4a), implying Nanjing is generally under the control of the Western Pacific  
619 subtropical high and can hardly be affected by the typhoon system. As a typical city in the  
620 northwest inland area of the YRD region (NIR), Nanjing is located far away from the sea, which  
621 means it may not be easily affected by the peripheral circulation of the typhoon system.

622         Additionally, at the altitude of 500 m and 1500 m above Shanghai, Nanjing, and Hangzhou  
623 (not shown), CHEM is also the major contributor to O<sub>3</sub> formation, with the values a litter lower  
624 than those at the surface, suggesting that there are strong photochemical reactions in the whole  
625 boundary layer of these YRD cities. In contrast, VDIF has an opposite effect in the middle of the  
626 boundary layer, with the negative contributions for O<sub>3</sub> of -3.26 ppb/h in Shanghai, -2.37 ppb/h in  
627 Hangzhou, and -3.21 ppb/h in Nanjing, respectively (not shown). The loss of O<sub>3</sub> at higher  
628 atmospheric level caused by VDIF further proves the essential role of the downward vertical  
629 movement in this O<sub>3</sub> episode.

630



631

632 **Fig. 9. Variations of the daytime mean values for the contributions of individual processes to O<sub>3</sub> formation in**  
 633 **(a) Shanghai, (b) Hangzhou, and (c) Nanjing from August 4 to 15 2013 at the surface layer. The contributors**  
 634 **include the total advection (TADV), the horizontal diffusion (HDIF), the vertical diffusion (VDIF), the**  
 635 **gas-phase chemistry (CHEM), the dry deposition (DDEP), and the cloud processes with the aqueous**  
 636 **chemistry (CLDS).**

637

#### 638 4.3.2 Spatial distribution of the contributors for the O<sub>3</sub> episode over the YRD region

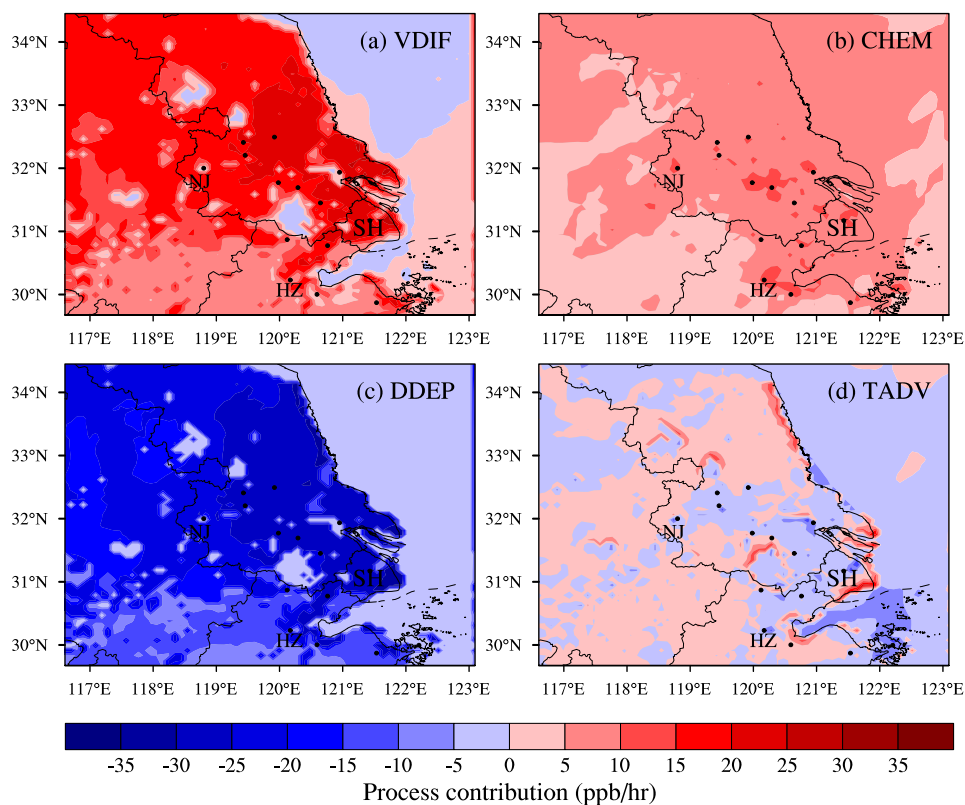
639 Fig. 10 demonstrates the spatial distribution of the daytime mean contributions of main

640 processes (VDIF, CHEM, DDEP and TADV) to the ozone formation at the lowest modeling layer  
641 in domain 3 during this high-level O<sub>3</sub> episode. The modeling results from 7 to 12 August are  
642 averaged to provide the mean values.

643         Similar to the results shown in Fig. 9, Fig. 10 illustrates that the vertical diffusion (VDIF) and  
644 the gas-phase chemistry (CHEM) exhibit significant positive contributions to O<sub>3</sub> over the YRD  
645 region and the surrounding areas during the high-level O<sub>3</sub> episode. The contributions of VDIF in  
646 domain 3 (Fig. 10a) range from 5 to 25 ppb/h, with the high values (> 20 ppb/h) occurring in the  
647 southeast coastal areas. For CHEM (Fig. 10b), the contributions vary within the range of 0-15  
648 ppb/h, with the high values over 10 ppb/h appearing in and around the big cities. As discussed  
649 above, these regional positive contributions of VDIF and CHEM over domain 3 should be related  
650 to the facts that the whole region is under the control of the Western Pacific subtropical high. With  
651 respect to the higher contributions of CHEM in the urban areas, they should be attributed to the  
652 spatial distribution of the emissions of O<sub>3</sub> precursors, which is also higher in the cities.  
653 Furthermore, higher air temperature in the cities related with the urban heat island may enhance  
654 the chemical reactions and form more O<sub>3</sub> in these areas as well.

655         For DDEP, it is the main critical factor of the consumption of O<sub>3</sub>, with the negative  
656 contributions varying from 0 to -25 ppb/h over the modeling domain 3 (Fig. 10c). Small values  
657 usually occur on the water, which may be related with less air pollution over rivers, lakes and  
658 oceans. High values can be found on land, especially in the southeast coastal areas. For the  
659 contributions of TADV, the values in domain 3 range from -10 to 10 ppb/h, with the positive  
660 contributions generally occurring on land while the negative ones appearing on the water (Fig.  
661 10d). The maximum positive contributions of TADV are usually found along the boundary  
662 between the land and the water, which should be explained by the facts that the land-sea breeze  
663 circulations can play an important role in the redistribution of the formed O<sub>3</sub>. On account of the  
664 high-pressure system and so-caused sinking airflows in the YRD region, the background wind is  
665 relatively weak in comparison to the local atmospheric circulation, thus the sea breeze can easily  
666 bring more generated O<sub>3</sub> to the seashore.

667



668

669 **Fig. 10. The daytime mean contributions of main processes to O<sub>3</sub> formation over the YRD region, including**  
 670 **(a) vertical diffusion (VDIF), (b) gas chemistry (CHEM), (c) dry deposition (DDEP), and (d) total advection**  
 671 **(TADV). The values are averaged from August 7 to 12 2013.**

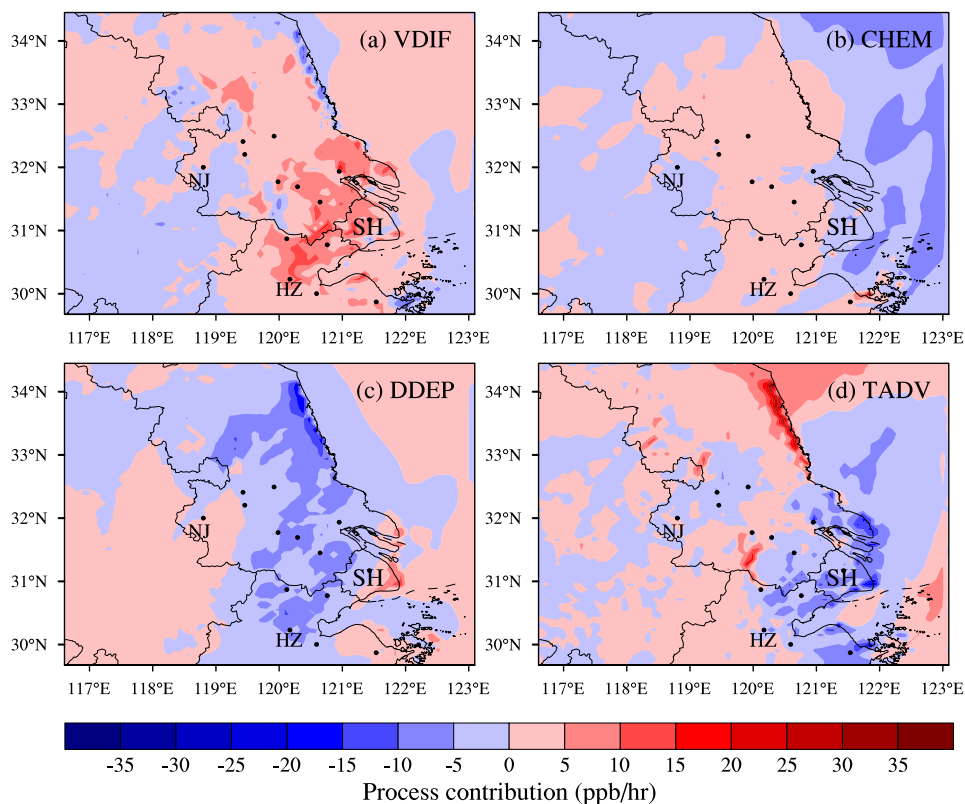
672

673

674 From the discussion in Section 3 and 4.2, it can be deduced that typhoon Utor plays an  
 675 important role in the formation of ozone over the YRD region during August 10-12. To clearly  
 676 clarify the effect of the typhoon system in this O<sub>3</sub> pollution episode, we firstly average the  
 677 modeling results of VDIF, CHEM, DDEP and TADV during August 10-12 to show their  
 678 contributions to O<sub>3</sub> formation when the typhoon system plays an important role. Secondly, the  
 679 modeling results of these processes from August 7 to 9 are also averaged to provide their  
 680 contributions when only the subtropical high dominates the episode. Finally, the differences of the  
 681 contributions of VDIF, CHEM, DDEP and TADV between the period of August 7-9 and August  
 682 10-12 are calculated to reveal the role of the typhoon system in this severe high O<sub>3</sub> episode (Fig.  
 683 11). As shown in Fig. 11a, when YRD is affected by the peripheral circulation of Typhoon Utor,  
 684 the contributions of VDIF over the YRD region increase by 0-15 ppb/h, with the higher increment  
 685 values (> 30 ppb/h) occurring in the southeast coastal region (SCR) and center inland region (CIR),

686 implying that SCR and CIR can be largely affected by the peripheral subsidence airflows of the  
 687 typhoon system. As to the contributions of CHEM, the increases caused by the typhoon system are  
 688 0-5 ppb/h over the YRD region, and the higher increment also appears in the coastal areas (Fig.  
 689 11b). For DDEP, influenced by typhoon Utor, its negative contributions decrease by up to -20  
 690 ppb/h, with the largest reduction along the coastline (Fig. 11c). For TADV, with the approaching of  
 691 typhoon Utor, the contributions of TADV particularly decrease by 0-20 ppb/h, especially in the  
 692 southeast coastal region (Fig. 11d).

693 In all, during this high-level O<sub>3</sub> pollution episode, more active photochemical reactions and  
 694 the vertical diffusion play a significant role in the accumulation of surface O<sub>3</sub> over the YRD region.  
 695 The major driving factor should be the Western Pacific subtropical high. Moreover, the changes in  
 696 the contributions of VDIF, CHEM, DDEP, and TADV between August 7-9 and August 10-12  
 697 exhibit a similar spatial pattern with the high values mostly concentrating in the southeast coastal  
 698 areas (Fig. 12), implying the Typhoon Utor also plays a collaborative effect.  
 699



700  
 701 **Fig. 11. The difference of daytime mean contributions of main processes to O<sub>3</sub> formation over the YRD**  
 702 **region between the period of August 10-12 and August 7-9, including (a) vertical diffusion (VDIF), (b) gas**  
 703 **chemistry (CHEM), (c) dry deposition (DDEP), and (d) total advection (TADV) .**

704

## 705 **5. Conclusions**

706 In this study, the characteristics and the essential impact factors of a typical regional  
707 continuous O<sub>3</sub> pollution over the YRD region are investigated by means of observational analysis  
708 and numerical simulation. The episode lasted for nearly a week from August 7 to 12 2013, with  
709 the O<sub>3</sub> concentration exceeding the national air quality standard in more than half of the cities over  
710 the YRD region. The analysis of weather systems and the modeling results from WRF/CMAQ all  
711 illustrate that the continuous strong Western Pacific subtropical high is the leading factor of the  
712 abnormally high temperature weather and the heavy O<sub>3</sub> pollution, by inducing more sinking air to  
713 trap heat as well as air pollutants at the surface. Meanwhile, the development of this episode is  
714 closely related to the movement of Typhoon Utor as well. The temporal variations of the vertical  
715 wind velocity and O<sub>3</sub> concentrations show that when the YRD region is at the front of moving  
716 typhoon system, the downward airflow is enhanced in the boundary layer with fine weather, and  
717 thereby the air pollutants are trapped and accumulated near the surface. Moreover, in the last stage  
718 of the O<sub>3</sub> episode, the activity of Typhoon Utor weakens the strength of the subtropical high and  
719 forces it to retreat easterly and move northward, and the prevailing southeasterly surface wind  
720 related with the approaching of Typhoon Utor contributes to the mitigation of the O<sub>3</sub> pollution.

721 The Integrated Process Rate (IPR) analysis implemented in CMAQ is specially carried out to  
722 quantify the relative contributions of individual processes and give a fundamental explanation.  
723 During the high-level O<sub>3</sub> episode from August 7-12, the vertical diffusion (VDIF) and the  
724 gas-phase chemistry (CHEM) exhibit significant positive contributions to surface O<sub>3</sub> over the  
725 YRD region, with the high values over 20 ppb/h for VDIF and over 10 ppb/h for CHEM. The dry  
726 deposition (DDEP) is the major sink of surface O<sub>3</sub>, while the total advection (TADV) can give the  
727 positive contribution on land and the negative contribution on the water. Moreover, on August  
728 10-12, the YRD region is apparently affected by the periphery circulation of Typhoon Utor, with  
729 the contributions of VDIF over the YRD region increasing by 0-15 ppb/h, the contributions of  
730 CHEM increasing by 0-5 ppb/h, and the contributions of DDEP and TADV decreasing. Especially  
731 in the coastal cities, such as Shanghai and Hangzhou, the effects of the typhoon system are more  
732 obvious. In contrast, the cities in the northwest inland area of the YRD region, which are far away  
733 from the sea, can hardly be affected by the typhoon system. In the end, when the typhoon system

734 significantly weakens the high pressure system, the contributions of VDIF, CHEM, TADV, and  
735 DDEP decrease to a low level in all cities.

736 The WRF/CMAQ modeling system shows a relatively good performance in simulation of the  
737 O<sub>3</sub> episode, with the simulated meteorological conditions and air pollutant concentrations  
738 basically in agreement with the observations in most YRD cities. Our results in this study can  
739 provide an insight for the formation mechanism of regional O<sub>3</sub> pollution in East Asia, and help to  
740 forecast the O<sub>3</sub> pollution synthetically impacted by the Western Pacific subtropical high and the  
741 tropical cyclone system.

742

### 743 **Acknowledgments**

744 This study was supported by the National Natural Science Foundation of China (41475122,  
745 91544230, 41575145), the National Special Fund for Environmental Protection Research in the  
746 Public Interest (201409008), EU 7th Framework Marie Curie Actions IRSES project REQUA  
747 (PIRSES-GA-2013-612671), and the National Science Foundation of Jiangsu Province  
748 (BE2015151). The authors would like to thank Hongli Wang from Shanghai Academy of  
749 Environmental Sciences for providing VOCs observation data, Xiaoxun Xie for preliminary data  
750 processing, and the anonymous reviewers for their constructive and precious comments on this  
751 manuscript.

752

### 753 **References**

- 754 An, X., Zhu, T., Wang, Z., Li, C., and Wang, Y.: A modeling analysis of a heavy air pollution episode occurred in  
755 Beijing, *Atmos Chem Phys*, 7, 3103-3114, 2007.
- 756 Byun, D., and Schere, K. L.: Review of the governing equations, computational algorithms, and other components  
757 of the models-3 Community Multiscale Air Quality (CMAQ) modeling system, *Appl Mech Rev*, 59, 51-77,  
758 10.1115/1.2128636, 2006.
- 759 Chan, C. K., and Yao, X.: Air pollution in mega cities in China, *Atmos Environ*, 42, 1-42,  
760 10.1016/j.atmosenv.2007.09.003, 2008.
- 761 Chen, F., and Dudhia, J.: Coupling an advanced land surface-hydrology model with the Penn State-NCAR MM5  
762 modeling system. Part I: Model implementation and sensitivity, *Mon Weather Rev*, 129, 569-585, Doi  
763 10.1175/1520-0493(2001)129<0569:Caalsh>2.0.Co;2, 2001.
- 764 Chen, D., Zhou, B., Beirle, S., Chen, L. M., and Wagner, T.: Tropospheric NO<sub>2</sub> column densities deduced from  
765 zenith-sky DOAS measurements in Shanghai, China, and their application to satellite validation, *Atmos Chem*  
766 *Phys*, 9, 3641-3662, 2009.
- 767 Cheng, W. L., Lai, L. W., Den, W., Wu, M. T., Hsueh, C. A., Lin, P. L., Pai, C. L., and Yan, Y. L.: The



768 relationship between typhoons' peripheral circulation and ground-level ozone concentrations in central Taiwan,  
769 Environ Monit Assess, 186, 791-804, 10.1007/s10661-013-3417-7, 2014.

770 Chiqueto, J., Silva, M. E. S.: São Paulo "Surface Ozone Layer" and the atmosphere: characteristics of tropospheric  
771 ozone concentrations in the city and how the atmosphere influences them, VDM Verlag Dr. Muller,  
772 Saarbrücken, 2010.

773 Ding, A. J., Fu, C. B., Yang, X. Q., Sun, J. N., Zheng, L. F., Xie, Y. N., Herrmann, E., Nie, W., Petaja, T.,  
774 Kerminen, V. M., and Kulmala, M.: Ozone and fine particle in the western Yangtze River Delta: an overview  
775 of 1 yr data at the SORPES station, Atmos Chem Phys, 13, 5813-5830, 10.5194/acp-13-5813-2013, 2013.

776 Duan, J. C., Tan, J. H., Yang, L., Wu, S., and Hao, J. M.: Concentration, sources and ozone formation potential of  
777 volatile organic compounds (VOCs) during ozone episode in Beijing, Atmos Res, 88, 25-35,  
778 10.1016/j.atmosres.2007.09.004, 2008.

779 Emmons, L. K., Walters, S., Hess, P. G., Lamarque, J. F., Pfister, G. G., Fillmore, D., Granier, C., Guenther, A.,  
780 Kinnison, D., Laepple, T., Orlando, J., Tie, X., Tyndall, G., Wiedinmyer, C., Baughcum, S. L., and Kloster, S.:  
781 Description and evaluation of the Model for Ozone and Related chemical Tracers, version 4 (MOZART-4),  
782 Geosci Model Dev, 3, 43-67, 2010.

783 Fann, N., and Risley, D.: The public health context for PM<sub>2.5</sub> and ozone air quality trends, Air Qual Atmos Hlth, 6,  
784 1-11, 10.1007/s11869-010-0125-0, 2013.

785 Feng, Z. W., Jin, M. H., Zhang, F. Z., and Huang, Y. Z.: Effects of ground-level ozone (O<sub>3</sub>) pollution on the  
786 yields of rice and winter wheat in the Yangtze River Delta, J Environ Sci-China, 15, 360-362, 2003.

787 Foley, K. M., Roselle, S. J., Appel, K. W., Bhawe, P. V., Pleim, J. E., Otte, T. L., Mathur, R., Sarwar, G., Young, J.  
788 O., Gilliam, R. C., Nolte, C. G., Kelly, J. T., Gilliland, A. B., and Bash, J. O.: Incremental testing of the  
789 Community Multiscale Air Quality (CMAQ) modeling system version 4.7, Geosci Model Dev, 3, 205-226,  
790 2010.

791 Gao, J. H., Bin, Z., Xiao, H., Kang, H. Q., Hou, X. W., and Shao, P.: A case study of surface ozone source  
792 apportionment during a high concentration episode, under frequent shifting wind conditions over the Yangtze  
793 River Delta, China, Sci Total Environ, 544, 853-863, 10.1016/j.scitotenv.2015.12.039, 2016.

794 Geng, F. H., Tie, X. X., Xu, J. M., Zhou, G. Q., Peng, L., Gao, W., Tang, X., and Zhao, C. S.: Characterizations of  
795 ozone, NO<sub>x</sub>, and VOCs measured in Shanghai, China, Atmos Environ, 42, 6873-6883,  
796 10.1016/j.atmosenv.2008.05.045, 2008.

797 Goncalves, M., Jimenez-Guerrero, P., and Baldasano, J. M.: Contribution of atmospheric processes affecting the  
798 dynamics of air pollution in South-Western Europe during a typical summertime photochemical episode,  
799 Atmos Chem Phys, 9, 849-864, 2009.

800 Grell, G. A., and Devenyi, D.: A generalized approach to parameterizing convection combining ensemble and data  
801 assimilation techniques, Geophys Res Lett, 29, Artn 169310.1029/2002gl015311, 2002.

802 Guo, H., Jiang, F., Cheng, H. R., Simpson, I. J., Wang, X. M., Ding, A. J., Wang, T. J., Saunders, S. M., Wang, T.,  
803 Lam, S. H. M., Blake, D. R., Zhang, Y. L., and Xie, M.: Concurrent observations of air pollutants at two sites  
804 in the Pearl River Delta and the implication of regional transport, Atmos Chem Phys, 9, 7343-7360, 2009.

805 Han, S. Q., Bian, H., Feng, Y. C., Liu, A. X., Li, X. J., Zeng, F., and Zhang, X. L.: Analysis of the Relationship  
806 between O<sub>3</sub>, NO and NO<sub>2</sub> in Tianjin, China, Aerosol Air Qual Res, 11, 128-139, 10.4209/aaqr.2010.07.0055,  
807 2011.

808 Hong, S. Y., Dudhia, J., and Chen, S. H.: A revised approach to ice microphysical processes for the bulk  
809 parameterization of clouds and precipitation, Mon Weather Rev, 132, 103-120, Doi  
810 10.1175/1520-0493(2004)132<0103:Aratim>2.0.Co;2, 2004.

811 Hong, S. Y., Noh, Y., and Dudhia, J.: A new vertical diffusion package with an explicit treatment of entrainment

812 processes, *Mon Weather Rev*, 134, 2318-2341, Doi 10.1175/Mwr3199.1, 2006.

813 Huang, J. P., Fung, J. C. H., Lau, A. K. H., and Qin, Y.: Numerical simulation and process analysis of  
814 typhoon-related ozone episodes in Hong Kong, *J Geophys Res-Atmos*, 110, Artn  
815 D0530110.1029/2004jd004914, 2005.

816 Huang, J. P., Fung, J. C. H., and Lau, A. K. H.: Integrated processes analysis and systematic meteorological  
817 classification of ozone episodes in Hong Kong, *J Geophys Res-Atmos*, 111, Artn  
818 D2030910.1029/2005jd007012, 2006.

819 Hung, C. H., and Lo, K. C.: Relationships between Ambient Ozone Concentration Changes in Southwestern  
820 Taiwan and Invasion Tracks of Tropical Typhoons, *Adv Meteorol*, Artn 40297610.1155/2015/402976, 2015.

821 Jenkin, M. E., and Clemitshaw, K. C.: Ozone and other secondary photochemical pollutants: chemical processes  
822 governing their formation in the planetary boundary layer, *Atmos Environ*, 34, 2499-2527, Doi  
823 10.1016/S1352-2310(99)00478-1, 2000.

824 Jiang, F., Wang, T. J., Wang, T. T., Xie, M., and Zhao, H.: Numerical modeling of a continuous photochemical  
825 pollution episode in Hong Kong using WRF-chem, *Atmos Environ*, 42, 8717-8727,  
826 10.1016/j.atmosenv.2008.08.034, 2008.

827 Jiang, F., Zhou, P., Liu, Q., Wang, T. J., Zhuang, B. L., and Wang, X. Y.: Modeling tropospheric ozone formation  
828 over East China in springtime, *J Atmos Chem*, 69, 303-319, 10.1007/s10874-012-9244-3, 2012.

829 Kim, H. J., and Wang, B.: Sensitivity of the WRF Model Simulation of the East Asian Summer Monsoon in 1993  
830 to Shortwave Radiation Schemes and Ozone Absorption, *Asia-Pac J Atmos Sci*, 47, 167-180,  
831 10.1007/s13143-011-0006-y, 2011.

832 Lam, K. S., Wang, T. J., Wu, C. L., and Li, Y. S.: Study on an ozone episode in hot season in Hong Kong and  
833 transboundary air pollution over Pearl River Delta region of China, *Atmos Environ*, 39, 1967-1977,  
834 10.1016/j.atmosenv.2004.11.023, 2005.

835 Landry, J. S., Neilson, E. T., Kurz, W. A., and Percy, K. E.: The impact of tropospheric ozone on landscape-level  
836 merchantable biomass and ecosystem carbon in Canadian forests, *Eur J Forest Res*, 132, 71-81,  
837 10.1007/s10342-012-0656-z, 2013.

838 Li, L., Chen, C. H., Huang, C., Huang, H. Y., Zhang, G. F., Wang, Y. J., Chen, M. H., Wang, H. L., Chen, Y. R.,  
839 Streets, D. G., and Fu, J. M.: Ozone sensitivity analysis with the MM5-CMAQ modeling system for Shanghai,  
840 *J Environ Sci-China*, 23, 1150-1157, 10.1016/S1001-0742(10)60527-X, 2011.

841 Li, L., Chen, C. H., Huang, C., Huang, H. Y., Zhang, G. F., Wang, Y. J., Wang, H. L., Lou, S. R., Qiao, L. P.,  
842 Zhou, M., Chen, M. H., Chen, Y. R., Streets, D. G., Fu, J. S., and Jang, C. J.: Process analysis of regional  
843 ozone formation over the Yangtze River Delta, China using the Community Multi-scale Air Quality modeling  
844 system, *Atmos Chem Phys*, 12, 10971-10987, 10.5194/acp-12-10971-2012, 2012.

845 Li, M. M., Song, Y., Huang, X., Li, J. F., Mao, Y., Zhu, T., Cai, X. H., and Liu, B.: Improving mesoscale modeling  
846 using satellite-derived land surface parameters in the Pearl River Delta region, China, *J Geophys Res-Atmos*,  
847 119, 6325-6346, 10.1002/2014JD021871, 2014.

848 Li, M. M., Song, Y., Mao, Z. C., Liu, M. X., and Huang, X.: Impacts of thermal circulations induced by  
849 urbanization on ozone formation in the Pearl River Delta region, China, *Atmos Environ*, 127, 382-392,  
850 10.1016/j.atmosenv.2015.10.075, 2016.

851 Liao, J. B., Wang, T. J., Wang, X. M., Xie, M., Jiang, Z. Q., Huang, X. X., and Zhu, J. L.: Impacts of different  
852 urban canopy schemes in WRF/Chem on regional climate and air quality in Yangtze River Delta, China,  
853 *Atmos Res*, 145, 226-243, 10.1016/j.atmosres.2014.04.005, 2014.

854 Liao, J. B., Wang, T. J., Jiang, Z. Q., Zhuang, B. L., Xie, M., Yin, C. Q., Wang, X. M., Zhu, J. L., Fu, Y., and  
855 Zhang, Y.: WRF/Chem modeling of the impacts of urban expansion on regional climate and air pollutants in

856 Yangtze River Delta, China, *Atmos Environ*, 106, 204-214, 10.1016/j.atmosenv.2015.01.059, 2015.

857 Liu, X. H., Zhang, Y., Xing, J., Zhang, Q. A., Wang, K., Streets, D. G., Jang, C., Wang, W. X., and Hao, J. M.:  
858 Understanding of regional air pollution over China using CMAQ, part II. Process analysis and sensitivity of  
859 ozone and particulate matter to precursor emissions, *Atmos Environ*, 44, 3719-3727,  
860 10.1016/j.atmosenv.2010.03.036, 2010.

861 Liu, Q., Lam, K. S., Jiang, F., Wang, T. J., Xie, M., Zhuang, B. L., and Jiang, X. Y.: A numerical study of the  
862 impact of climate and emission changes on surface ozone over South China in autumn time in 2000-2050,  
863 *Atmos Environ*, 76, 227-237, 10.1016/j.atmosenv.2013.01.030, 2013.

864 Lou, S. J., Liao, H., and Zhu, B.: Impacts of aerosols on surface-layer ozone concentrations in China through  
865 heterogeneous reactions and changes in photolysis rates, *Atmos Environ*, 85, 123-138,  
866 10.1016/j.atmosenv.2013.12.004, 2014.

867 Lu, W. Z., and Wang, X. K.: Evolving trend and self-similarity of ozone pollution in central Hong Kong ambient  
868 during 1984-2002, *Sci Total Environ*, 357, 160-168, 10.1016/j.scitotenv.2005.03.015, 2006.

869 Ma, J. Z., Xu, X. B., Zhao, C. S., and Yan, P.: A review of atmospheric chemistry research in China:  
870 Photochemical smog, haze pollution, and gas-aerosol interactions, *Adv Atmos Sci*, 29, 1006-1026,  
871 10.1007/s00376-012-1188-7, 2012.

872 Mlawer, E. J., Taubman, S. J., Brown, P. D., Iacono, M. J., and Clough, S. A.: Radiative transfer for  
873 inhomogeneous atmospheres: RRTM, a validated correlated-k model for the longwave, *J Geophys Res-Atmos*,  
874 102, 16663-16682, Doi 10.1029/97jd00237, 1997.

875 Monin, A. S., Obukhov, A.M.: Basic laws of turbulent mixing in the surface layer of the atmosphere,  
876 *Contributions of the Geophysical Institute of the Slovak Academy of Sciences* 151, 163-187, 1954.

877 Peng, J. B.: An Investigation of the Formation of the Heat Wave in Southern China in Summer 2013 and the  
878 Relevant Abnormal Subtropical High Activities, *Atmospheric & Oceanic Science Letters*, 7, 286-290, 2014.

879 Ran, L., Zhao, C. S., Geng, F. H., Tie, X. X., Tang, X., Peng, L., Zhou, G. Q., Yu, Q., Xu, J. M., and Guenther, A.:  
880 Ozone photochemical production in urban Shanghai, China: Analysis based on ground level observations, *J*  
881 *Geophys Res-Atmos*, 114, Artn D1530110.1029/2008jd010752, 2009.

882 Shao, M., Zhang, Y. H., Zeng, L. M., Tang, X. Y., Zhang, J., Zhong, L. J., and Wang, B. G.: Ground-level ozone  
883 in the Pearl River Delta and the roles of VOC and NO<sub>x</sub> in its production, *J Environ Manage*, 90, 512-518,  
884 10.1016/j.jenvman.2007.12.008, 2009.

885 Shi, C. Z., Wang, S. S., Liu, R., Zhou, R., Li, D. H., Wang, W. X., Li, Z. Q., Cheng, T. T., and Zhou, B.: A study  
886 of aerosol optical properties during ozone pollution episodes in 2013 over Shanghai, China, *Atmos Res*, 153,  
887 235-249, 10.1016/j.atmosres.2014.09.002, 2015.

888 Sillman, S.: The relation between ozone, NO<sub>x</sub> and hydrocarbons in urban and polluted rural environments, *Atmos*  
889 *Environ*, 33, 1821-1845, Doi 10.1016/S1352-2310(98)00345-8, 1999.

890 State Environmental Protection Administration of China: China National Environmental Protection Standard:  
891 Automated Methods for Ambient Air Quality Monitoring, China Environmental Science Press, Beijing, 2006.

892 Tang, W. Y., Zhao, C. S., Geng, F. H., Peng, L., Zhou, G. Q., Gao, W., Xu, J. M., and Tie, X. X.: Study of ozone  
893 "weekend effect" in Shanghai, *Sci China Ser D*, 51, 1354-1360, 10.1007/s11430-008-0088-2, 2008.

894 Tang, G., Li, X., Wang, Y., Xin, J., and Ren, X.: Surface ozone trend details and interpretations in Beijing,  
895 2001-2006, *Atmos Chem Phys*, 9, 8813-8823, 2009.

896 Tu, J., Xia, Z. G., Wang, H. S., and Li, W. Q.: Temporal variations in surface ozone and its precursors and  
897 meteorological effects at an urban site in China, *Atmos Res*, 85, 310-337, 10.1016/j.atmosres.2007.02.003,  
898 2007.

899 Wang, H. L., Chen, C. H., Wang, Q., Huang, C., Su, L. Y., Huang, H. Y., Lou, S. R., Zhou, M., Li, L., and Qiao, L.

900 P.: Chemical loss of volatile organic compounds and its impact on the source analysis through a two-year  
901 continuous measurement, *Atmospheric Environment*, 80, 488-498, 2013.

902 Wang, H. X., Zhou, L. J., and Tang, X. Y.: Ozone concentrations in rural regions of the Yangtze Delta in China, *J*  
903 *Atmos Chem*, 54, 255-265, 10.1007/s10874-006-9024-z, 2006a.

904 Wang, T. J., Lam, K. S., Xie, M., Wang, X. M., Carmichael, G., and Li, Y. S.: Integrated studies of a  
905 photochemical smog episode in Hong Kong and regional transport in the Pearl River Delta of China, *Tellus B*,  
906 58, 31-40, 10.1111/j.1600-0889.2005.00172.x, 2006b.

907 Wang, X. M., Lin, W. S., Yang, L. M., Deng, R. R., and Lin, H.: A numerical study of influences of urban  
908 land-use change on ozone distribution over the Pearl River Delta region, China, *Tellus B*, 59, 633-641,  
909 10.1111/j.1600-0889.2007.00271.x, 2007.

910 Wang, T., Wei, X. L., Ding, A. J., Poon, C. N., Lam, K. S., Li, Y. S., Chan, L. Y., and Anson, M.: Increasing  
911 surface ozone concentrations in the background atmosphere of Southern China, 1994-2007, *Atmos Chem Phys*,  
912 9, 6217-6227, 2009a.

913 Wang, X. M., Chen, F., Wu, Z. Y., Zhang, M. G., Tewari, M., Guenther, A., and Wiedinmyer, C.: Impacts of  
914 Weather Conditions Modified by Urban Expansion on Surface Ozone: Comparison between the Pearl River  
915 Delta and Yangtze River Delta Regions, *Adv Atmos Sci*, 26, 962-972, 10.1007/s00376-009-8001-2, 2009b.

916 Wei, X. L., Liu, Q., Lam, K. S., and Wang, T. J.: Impact of precursor levels and global warming on peak ozone  
917 concentration in the Pearl River Delta Region of China, *Adv Atmos Sci*, 29, 635-645,  
918 10.1007/s00376-011-1167-4, 2012.

919 Xie, M., Wang, T.J., Jiang, F., Yang, X.Q.: Modeling of natural NO<sub>x</sub> and VOC emissions and their effects on  
920 tropospheric photochemistry in China, *Environ. Sci. China*, 28, 31-40, 2007.

921 Xie, M., Li, S., Jiang, F., and Wang, T. J.: Methane emissions from terrestrial plants over China and their effects  
922 on methane concentrations in lower troposphere, *Chinese Sci Bull*, 54, 304-310, 10.1007/s11434-008-0402-6,  
923 2009.

924 Xie, M., Zhu, K. G., Wang, T. J., Yang, H. M., Zhuang, B. L., Li, S., Li, M. G., Zhu, X. S., and Ouyang, Y.:  
925 Application of photochemical indicators to evaluate ozone nonlinear chemistry and pollution control  
926 countermeasure in China, *Atmos Environ*, 99, 466-473, 10.1016/j.atmosenv.2014.10.013, 2014.

927 Xie, M., Liao, J., Wang, T., Zhu, K., Zhuang, B., Han, Y., Li, M., Li, S.: Modeling of the anthropogenic heat flux  
928 and its effect on regional meteorology and air quality over the Yangtze River Delta region, China, *Atmos.*  
929 *Chem. Phys.*, 16, 6071-6089, 10.5194/acp-16-6071-2016, 2016a.

930 Xie, M., Zhu, K. G., Wang, T. J., Chen, P. L., Han, Y., Li, S., Zhuang, B. L., and Shu, L.: Temporal  
931 characterization and regional contribution to O<sub>3</sub> and NO<sub>x</sub> at an urban and a suburban site in Nanjing, China,  
932 *Sci Total Environ*, 551, 533-545, 10.1016/j.scitotenv.2016.02.047, 2016b.

933 Yarwood, G., Rao, S., Yocke, M., Whitten G.: Updates to the Carbon Bond chemical mechanism: CB05., Final  
934 Report to the U.S. EPA, RT-0400675, 2005.

935 Zhang, X. Y., Zhang, P., Zhang, Y., Li, X. J., and Qiu, H.: The trend, seasonal cycle, and sources of tropospheric  
936 NO<sub>2</sub> over China during 1997-2006 based on satellite measurement, *Sci China Ser D*, 50, 1877-1884,  
937 10.1007/s11430-007-0141-6, 2007.

938 Zhang, Y. H., Su, H., Zhong, L. J., Cheng, Y. F., Zeng, L. M., Wang, X. S., Xiang, Y. R., Wang, J. L., Gao, D. F.,  
939 Shao, M., Fan, S. J., and Liu, S. C.: Regional ozone pollution and observation-based approach for analyzing  
940 ozone-precursor relationship during the PRIDE-PRD2004 campaign, *Atmos Environ*, 42, 6203-6218,  
941 10.1016/j.atmosenv.2008.05.002, 2008.

942 Zhang, Q., Streets, D. G., Carmichael, G. R., He, K. B., Huo, H., Kannari, A., Klimont, Z., Park, I. S., Reddy, S.,  
943 Fu, J. S., Chen, D., Duan, L., Lei, Y., Wang, L. T., and Yao, Z. L.: Asian emissions in 2006 for the NASA

- 944 INTEX-B mission, *Atmos Chem Phys*, 9, 5131-5153, 2009.
- 945 Zhu, B., Kang, H. Q., Zhu, T., Su, J. F., Hou, X. W., and Gao, J. H.: Impact of Shanghai urban land surface forcing  
946 on downstream city ozone chemistry, *J Geophys Res-Atmos*, 120, 4340-4351, 10.1002/2014JD022859, 2015.
- 947